Environmental Science Advances

PAPER

Check for updates
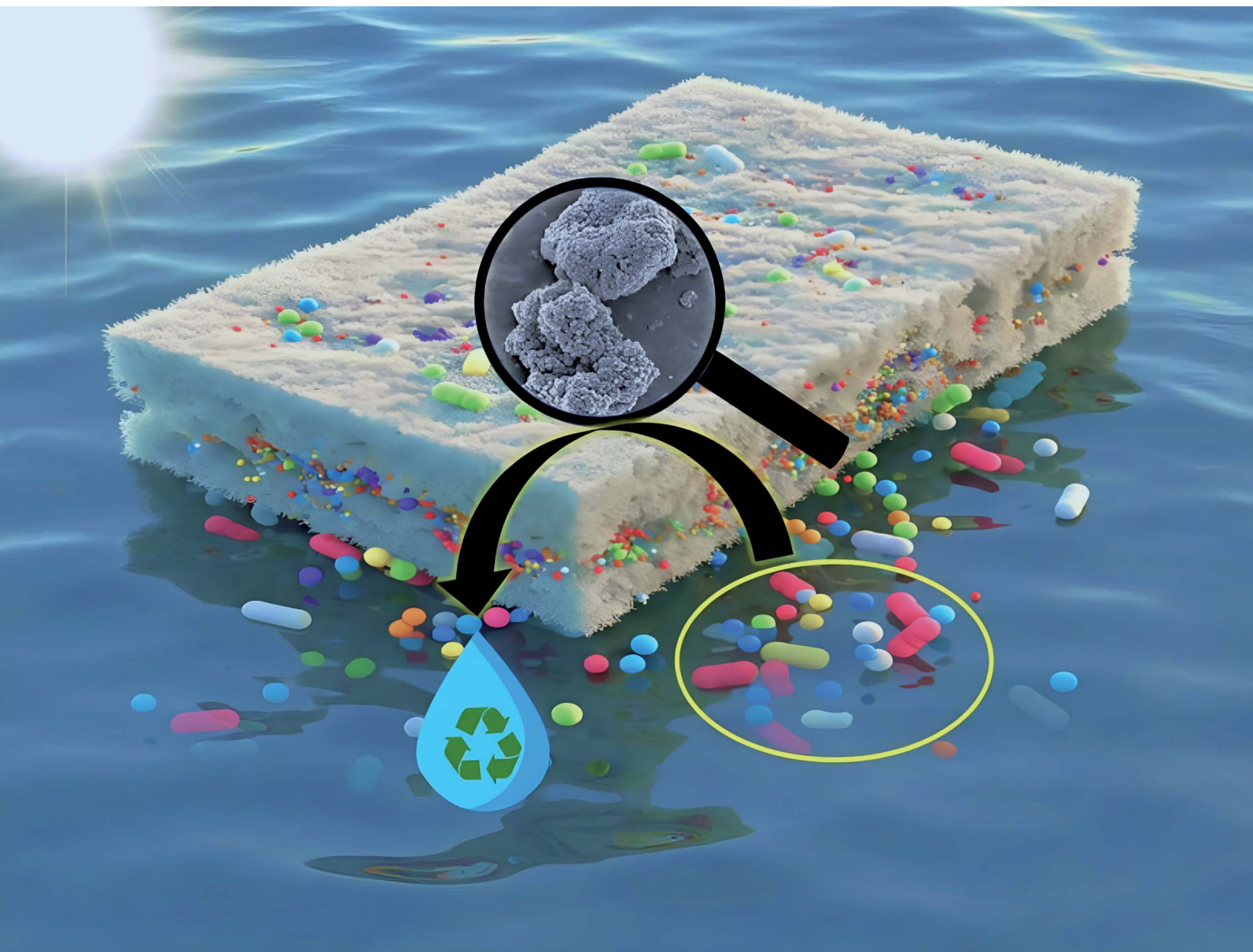
Functionalized 3D polyurethane foams with microwave-synthesized TiO₂ nanostructures for solar light-driven degradation of tetracycline†

Maria Leonor Matias, [a] Ana Pimentel, [a] Ana S. Reis Machado, [ab]
Joana Rodrigues, [c] Auguste Fernandes, [d] Teresa Monteiro, [c] Patrícia Almeida
Carvalho, [ef] Mariana N. Amaral, [gh] Catarina Pinto Reis, [gh]
Jonas Deuermeier, [a] Elvira Fortunato, [a] Rodrigo Martins *[a]
and Daniela Nunes *[a]

Pharmaceutical substances present in soils and water supplies pose a significant risk to the ecosystem. Solar light-driven photocatalysis with titanium dioxide (TiO₂) nanophotocatalysts has been widely explored for the degradation of these substances in aquatic resources. However, the lack of reported sustainable methods to produce TiO₂ nanophotocatalysts and the challenges associated with their use in powder form during photocatalytic experiments further limit their scale-up. Herein, we show an eco-friendly approach to synthesize TiO₂ nanopowders using a fast microwave method (10 min) and their further incorporation on polyurethane (PU) foams by a simple dip-coating process. Ethanol, isopropanol (IPA), and water were employed for the microwave synthesis of TiO₂ nanophotocatalysts, unveiling distinct structural and optical properties for the material synthesized in each solvent. When ethanol was used as a solvent, TiO₂ anatase nanocrystals were obtained, which exhibited high-index {012}/{102} facets with surface steps and bulk defects. These defects together with the superior specific surface area and higher capacity for surface oxygen adsorption contributed to a significant adsorption capacity (about 58% in 240 min) of tetracycline (TC) and overall TC removal of ~90% after 30 min of simulated solar light exposure. Reusable TiO₂-PU foams achieved ~80% of TC removal in 180 min of light exposure. This study showcases the successful surface modification of PU foams with TiO₂ nanostructures highlighting their potential for an efficient removal of tetracycline from water while ensuring ecological safety, as demonstrated by the ecotoxicity assays using the *Artemia salina* model.

Environmental significance

Wastewater recalcitrant contaminants, including antibiotics, pose a significant risk to human health and the ecosystem. In this regard, the utilization of solar-driven photocatalysts on sustainable platforms aims to avoid the issues of recovery and recyclability of powdered photocatalysts in photocatalytic experiments, while providing a promising and scalable strategy for the treatment of polluted effluents. Various solvents were investigated to produce TiO₂ nanostructures with distinct structural and optical properties through a fast and eco-friendly microwave approach. This approach in combination with a dip-coating technique gave rise to 3D porous and defective TiO₂ nanostructures on flexible polyurethane foams. The relationship between the structural defects and the nanomaterial's photocatalytic performance was evaluated for the degradation of tetracycline. Moreover, the produced platforms were reusable and aquatic life safe.

ᵃCENIMAT|i3N, Department of Materials Science, School of Science and Technology, NOVA University Lisbon and CEMOP/UNINOVA, 2829-516 Caparica, Portugal. E-mail: daniela.gomes@fct.unl.pt; rm@uninova.pt; Fax: +351 212948558; Tel: +351 212948562

ᵇLAQV-REQUIMTE, Department of Chemistry, NOVA School of Science and Technology, Universidade NOVA de Lisboa, Campus de Caparica, 2829-516 Caparica, Portugal

ᶜPhysics Department and i3N, Aveiro University, Campus Universitário de Santiago, 3810-193 Aveiro, Portugal

ᵈCentro de Química Estrutural, Instituto Superior Técnico, Universidade de Lisboa, Av. Rovisco Pais, 1049-001 Lisboa, Portugal

ᵉSINTEF, Material Physics, 0373 Oslo, Norway

ᶠCeFEMA, Instituto Superior Técnico, Universidade de Lisboa, Av. Rovisco Pais, 1049-001 Lisboa, Portugal

ᵍResearch Institute for Medicines (iMed.ULisboa), Faculty of Pharmacy, Universidade de Lisboa, Av. Professor Gama Pinto, 1649-003 Lisboa, Portugal

ʰInstituto de Biofísica e Engenharia Biomédica (IBEB), Faculdade de Ciências, Universidade de Lisboa, Campo Grande, 1749-016 Lisboa, Portugal

† Electronic supplementary information (ESI) available. See DOI: https://doi.org/10.1039/d4va00110a

© 2025 The Author(s). Published by the Royal Society of Chemistry

Environ. Sci.: Adv., 2025, **4**, 713–738 | **713**

Introduction

The presence of contaminants in water resources has increased worldwide due to the development of industrialization and intensive farming activities, negatively affecting human health and the ecosystem.[1,2] Although various water quality parameters are targeted in sewage treatment plants, such as turbidity, color and pH,[3] various toxic and recalcitrant organic and inorganic contaminants are constantly being released to aquatic systems, making the wastewater treatment of effluents an ecological challenge.[1,2] Typical organic contaminants found in effluents include antibiotics.[4] The sources of this type of pollution stem from pharmaceutical wastewater, human and veterinary antibiotics that are not completely metabolized and expired/unused antibiotics.[5] Numerous antibiotics are detected in aqueous systems worldwide, namely sulfonamides, tetracyclines, β-lactams and macrolides.[4] For instance, tetracyclines (TCs) are a broad spectrum of antibiotics that can treat several bacterial infections and other pathological conditions. This type of antibiotic is frequently administered in humans and animals and is also used as a feed additive in the agricultural sector.[6–8]

This class of antibiotics can be categorized into three groups according to the production method. They can be produced from strains of *Streptomyces* bacteria or by biosynthesis (*e.g.* chlortetracycline, oxytetracycline, and demeclocycline), through semi-synthetic methods (*e.g.* doxycycline, lymecycline, and meclocycline) or completely synthesized (*e.g.* tigecycline).[9–11] Tetracycline molecules comprise a hydronaphtacene framework with four linearly condensed benzene rings. The main differences between the tetracycline analogues are the substituents at the carbons in the positions 5, 6, 7 and 9.[12] They contain two different chromophoric regions and possess three pK_a values: pK_{a_1} (protonation of oxygen bound at the carbon position 3), pK_{a_2} (protonation of oxygen bound at the carbon positions 10 and 12) and pK_{a_3} (protonation of the dimethyl functional group at the carbon position 4) at pH values of 3.3, 7.7 and 9.7, respectively. Therefore, at pH values below pK_{a_1} they have cationic form, at pH between pK_{a_1} and pK_{a_2} they are neutral (zwitterionic state) and above pK_{a_3} they are anionic.[11,13,14]

Since the majority of pharmaceuticals exhibit low absorption rates in both humans and animals, a significant fraction is excreted without structural changes *via* feces or urine.[15] As a consequence, low concentrations of antibiotics accumulate in soils and reach aquatic environments,[15,16] thus threatening aquatic and terrestrial biodiversity.[17] Moreover, the long-term existence of antibiotics in the environment may induce antibiotic-resistant bacteria and antibiotic-resistance genes, leading to the spread of antibiotic resistance.[5,18,19] For that reason, it is imperative to remove these pollutants from the environment, encompassing water and soil, to mitigate their environmental impact.[20]

Several investigations have, however, focused on the development of sustainable technologies to improve water quality. Those technologies include physical, chemical and biological methods.[21,22] Inside these methods, each process possesses its advantages and disadvantages dependent on the option chosen, namely, the cost, effectiveness, operability, reliability, ecological footprint, pre-treatment requirements and the production of sludge and hazardous residues.[23]

Among these techniques, chemical methods and in particular advanced oxidation processes (AOPs) are effective for the degradation of water pollutants, including pharmaceutical residues.[24] The Fenton reaction, ozonation, photocatalytic oxidation and electrochemical oxidation are some of the processes included in AOPs.[25,26] In these AOPs, powerful oxidation agents (such as hydroxyl radical species) are generated with the ability to degrade the pollutants into smaller molecules or harmless products and can achieve complete mineralization of hazardous pollutants.[22,27] Moreover, AOPs are easy to use, provide fast reaction rates and can eliminate dissolved organic contaminants present in low concentrations that are challenging to remove.[28,29] Photocatalysis is a promising "green" AOP that can utilize solar energy to its fullest extent, while the removal of pollutants can be conducted under normal ambient conditions (temperature and pressure).[22]

Despite the numerous attempts to fabricate efficient photoactive materials, TiO_2 remains the benchmark photocatalyst,[30] providing strong oxidation potential for pollutant decomposition, physical and chemical stabilities, and reduced cost and toxicity.[31] Concerning the synthesis approaches, microwave irradiation has many advantages, such as high reaction yields in a shorter amount of time and less energy consumption than other conventional methods (*e.g.*, oven), good reproducibility, straightforward manipulation and control of the nanostructures' properties based on the microwave parameters. These attributes make it an ideal choice for the synthesis of nanomaterials.[32–34]

The mixture volume, solvents employed, reaction vessel size, power level and temperature are a few crucial microwave parameters that can affect the properties of the final material.[35,36] Previous studies have reported the effect of using different solvents on the microwave-assisted synthesis of TiO_2 nanostructures.[37–40] For instance, Jalawkhan and his group[38] performed a fast synthesis (5 min) of TiO_2 nanostructures in a commercial microwave oven (750 W) by using ethylene glycol (EG) or water and titanium isopropoxide (TTIP). The materials were subjected to a subsequent thermal annealing treatment at 400 °C for 1 h. The resultant TiO_2 nanopowders were composed of nanorods or spherical agglomerated particles when EG or water was employed as a solvent, respectively. The TiO_2 anatase crystalline phase was obtained in both cases, but Brunauer–Emmett–Teller (BET) analysis unveiled differences in the specific surface areas of the produced nanomaterials. In another study, different morphologies of TiO_2 nanostructures were obtained: beads, spindles, square platelets and porous spheres in a mixture of ethanol and water for the first two cases, and hydrofluoric acid (HF) and ethanol for the other cases, respectively. Regardless of the solvent used, only the pure TiO_2 anatase phase was identified. The TiO_2 precursor used was titanium butoxide and the microwave temperatures ranged from 180 to 200 °C. The utilization of these TiO_2 nanostructures as photoanodes revealed different power conversion efficiencies depending on their morphology.[39]

Table 1   Performance of several TiO$_2$-based photocatalyst systems on PU supports for the degradation of water pollutants

Photocatalyst	Immobilization of the nanostructures on PU *in situ?*	Light source	Photocatalytic conditions	Optimal degradation efficiency	Kinetic constant (min^{-1})	Reference
Iron–tetracarboxy phenyl porphyrin–sulphur–titanium dioxide–reduced graphene oxide (Fe–TCPP–S–TiO$_2$–rGO)	No	Solar light	• Pollutant: cyanide • Volume: 50 mL • Solution's concentration: 100 ppm • Quantity of photocatalyst: 100 mg	91% Degradation as well as 88% toxicity removal in 2 h	0.0196	61
Silver–titanium dioxide–graphene (Ag–commercial TiO$_2$ P25–G)	No	Visible light	• Pollutant: diesel • Solution's concentration: 15 000 ppm • Quantity of photocatalyst: 300 mg	76% of Degradation in 16 h	0.0017 (Deduced based on the experimental data)	44
Titanium dioxide (commercial TiO$_2$ P25)	No	UV light irradiation (λ = 254 nm, 18 mW cm^{-2})	• Pollutant: bisphenol A (BPA) • Solution's concentration: 10 ppm • Experiments were carried out in a self-designed horizontal circulating bed photocatalytic reactor (HCBPR) • The optimum ratio of the volume of PU foam to the effective reaction volume of HCBPR was 1%	97% Degradation in 6 h (95% removal of TOC)	0.003 (Deduced based on the experimental data)	42
Silicon dioxide–titanium dioxide (SiO$_2$/TiO$_2$)	No	UV light source <400 nm	• Pollutant: acid black 1 (AB 1) • Solution's concentration: 10 ppm • Total weight of the PU-SiO$_2$/TiO$_2$ film photocatalyst: 160 mg	100% of Degradation in 60 min PU-40% SiO$_2$/TiO$_2$ hybrid composite film	Not calculated	62

Another reported research study explored the effect of eight alcohol solvents, divided into two categories: primary and secondary/ternary alcohols, on TiO_2 anatase nanocrystals synthesized by a microwave approach at 220 °C for 30 min. Variations in both the crystallite size and shape were observed, contingent upon the type of solvent used. The highest photocatalytic performance was obtained by using isopropanol as a solvent owing to its tendency to crystallize preferentially on the anatase {001} facets.[40] This study also investigates how various solvents (ethanol, isopropanol and water) influence the formation of TiO_2 nanostructures. Nevertheless, a simple and fast microwave approach (10 min) without any pre- or post-treatment before or after microwave synthesis and without toxic reagents is carried out. Differences in terms of shape, size, structural defects and crystalline phase are also reported.

The effective utilization of photoactive materials in heterogeneous photocatalysis commonly requires powdered materials due to the higher surface-to-volume ratios and mass transfer rates.[41] Nonetheless, the recovery of these materials is difficult and costly to implement in large-scale processes, making the immobilization of photocatalysts on substrates an excellent alternative to avoid these issues.[42–44] Examples of those substrates include glass, polymers, textiles, and cork, among others.[45,46] More recently, researchers have developed an innovative class of photocatalysts, the "floating" photocatalysts. The fabrication of these photocatalysts has received considerable attention to address the limitations associated with non-buoyant photocatalysts, such as agglomeration, recovery and flexibility.[46]

Polyurethane (PU) is a thermoplastic polymer, easily adaptable to several industrial applications: tubing, footwear, industrial machinery, elastic fibers, insulators, medical devices, paints, and coatings, among others. This versatile material presents outstanding abrasion resistance, low density, flexibility at reduced temperatures and suitable properties (chemical, mechanical and physical).[44,47] It is composed of repeated urethane (–NHCOO–) basic units and fabricated through the exothermic reaction involving diisocyanate (O=C=N–R'–N=C=O) and either a polyester or a polyether polyol (HO–R–OH).[41] The utilization of nanoparticles to modify the chemical and mechanical properties of PU has proved to be effective in their enhancement.

Although PU recycling presents some challenges, primarily due to the chemically cross-linked structure of most PUs in the market (thermosets) and the diverse compositions of PUs mixed during waste disposal,[48] it has been demonstrated that polyurethanes can undergo chemical recycling, reverting to their constituent monomers or segments, and be utilized to generate new ones.[49] In this regard, research work is still in progress, but results indicate potential circular economy solutions for PU.[50] Therefore, the combination of nanoparticles with this polymer extends its applicability across an extensive range of research fields, for instance, photocatalysis, sensors, solar/fuel cells, biomedical materials and self-cleaning coatings.[47] PU foams, besides having a floating character, present a large surface area, high adsorption ability and excellent reusability.[44,51,52] Nanostructures can be directly embedded into the polymer matrix throughout the fabrication process of polyurethane foams or membranes.[44,53] Despite that, to expose the total surface of nanostructures to water pollutants, other alternatives are required. For instance, a possible strategy for the immobilization of nanostructures could be achieved by the chemical bath deposition (CBD) method[41] or by *in situ* synthesis of the nanostructures,[54] in which the latter can be combined with a PU's surface chemical treatment.[55] However, one technique that has shown promising results is dip-coating. Various studies have shown an effective functionalization of PU foams with nanoparticles by dip-coating. The simplicity, ability to scale up and use of inexpensive reagents are the main advantages of this method.[56–58]

Various studies have been performed with PU sponges as oil adsorbents,[51,59,60] but few studies have reported the photodegradation of water pollutants using reusable polyurethane foams immobilized with nano TiO_2-based photocatalysts. To compare the performance of different TiO_2-based photocatalysts on PU supports for the decomposition of water contaminants, Table 1 presents the studies that were found in the literature. Studies with missing data were not included in Table 1.

Encouraged by the lack of research work regarding the decontamination of wastewater using TiO_2 nanophotocatalysts immobilized on reusable polyurethane foams, and considering the potential that floating photocatalysts may bring to replace the conventional TiO_2 photocatalysts, herein we report the adsorption and photocatalytic performance of TiO_2 nanostructures immobilized on PU foams by dip-coating for the removal and degradation of tetracycline under solar light radiation. As far as the authors are aware, this has never been reported. The effect of ethanol, IPA and water on the formation of TiO_2 nanostructures by a simple and fast microwave approach (10 min) is also systematically studied, at the atomic level, demonstrating the direct relation between the structural defects and the nanomaterial's photocatalytic performance. In addition, we report the photocatalytic efficiency of the TiO_2 nanopowders synthesized with the three different solvents for the degradation of tetracycline. Recyclability tests were performed with TiO_2 nanopowders and 3D TiO_2 PU foams. Chemical quenching experiments are also presented for a comprehension of the photocatalytic mechanism. Moreover, we report the results of ecotoxicity experiments by evaluating the acute toxicity of PU foams (with and without TiO_2 nanostructures) to nauplii of *Artemia salina*.

Experimental section

Materials

Hydrochloric acid (HCL, 37% from Merck), titanium(IV) isopropoxide (TTIP, 97% from Sigma-Aldrich), polyacrylic acid (PAA, Mv ~450 000 from Sigma-Aldrich), sodium hydroxide (NaOH, 98% from PanReac AppliChem), commercial polyurethane foam ("Bio Filter Media Sponge", $\rho = 0.016$ g cm^{-3} and a number of pores per unit area of 35 pores per cm^2) from Shunting, tetracycline TC, ($C_{22}H_{24}N_2O_8$, 98% from Sigma-Aldrich), ethylene diamine tetra acetic acid (EDTA,

$C_{10}H_{16}N_2O_8$, ≥98% from Sigma-Aldrich), hydrogen peroxide (H_2O_2, >30% w/v from PanReac AppliChem), isopropanol (IPA, C_3H_8O, 99.8% from Sigma-Aldrich), p-benzoquinone (BQ, $C_6H_4O_2$, ≥98% from Sigma-Aldrich), sodium azide (NaN_3, Bio-Xtra, from Sigma-Aldrich), commercial seawater salt (JBL GmbH & Co., Neuhofen, Germany) and dimethyl sulfoxide (DMSO, ≥99.5% from Sigma-Aldrich). Ethanol (96% from PanReac AppliChem) and Millipore water were also used.

Synthesis of TiO$_2$ nanostructures using a microwave digestion system

TiO_2 nanostructures were obtained by a rapid microwave approach. A solution volume of 50 mL was prepared, in which 4 mL of HCL was mixed with 44.4 mL of different solvents (deionized water, ethanol, or IPA). Afterwards, 1.6 mL of TTIP was added dropwise to the previous mixture and it was left to stir for 10–20 min, or until a homogeneous solution was obtained. A CEM microwave digestion system (MARS one) was employed to conduct the microwave synthesis at 1000 W, 200 ± 10 °C for 10 min. Since each Teflon vessel has a capacity of 75 mL, 25 mL of solution volumes were distributed into 2 vessels. The resultant TiO_2 nanopowders were washed with Millipore water and ethanol multiple times using a centrifuge at 5300 rpm until the pH of the solution was 6–7. In the end, the nanopowders were kept in a desiccator and dried at 80 °C under vacuum for 12 hours. It is important to mention that the microwave-assisted syntheses are reproducible and the obtained weights were 0.43 g (% yield = 100%), 0.32 g (% yield ≈ 74%) and 0.15 g (% yield ≈ 35%) when ethanol, IPA and H_2O were used as solvents, respectively. From hereafter the TiO_2 nanostructures synthesized in ethanol, isopropanol and water will be denoted as TiO_2_EtOH, TiO_2_IPA and TiO_2_H_2O, respectively.

Incorporation of TiO$_2$ nanostructures into PU foams

The microwave-synthesized TiO_2 nanopowders (30 mg) were dispersed in 20 mL of Millipore water and ultrasonically agitated for 30 min (solution A), see step 1 in Fig. 1. A second solution (solution B) was prepared by mixing 10 mg of PAA with 20 mL of Millipore water. Solution B was left to stir for 30 min, see step 1 in Fig. 1. After that, solution B was poured into solution A and stirred magnetically. Then, the pH was adjusted with NaOH to 7,[63] see step 2 in Fig. 1. Commercial porous polyurethane foam was cut into parallelepipeds of 1.5 cm^3 by volume (0.5 cm height × 1 cm width × 3 cm length). The previously cut PU foams were cleaned for 15 min in deionized water using an ultrasonic bath to remove possible dirt.

Similarly to previous papers,[41,55] to improve the hydrophilicity, PU foams were pre-treated in a 1 M aq. solution of NaOH at 60 °C for 20 min, under agitation. This solution is going to etch away part of the cell windows within the foam structure, exposing hydrophilic groups.[64] To study the hydrophilicity of the PU sponges, pristine and pre-treated foams were immersed in distilled water for 30 s and left to dry for another 30 s at room temperature (RT) in a vertical position. PU foams were then weighed. After being soaked in water, the weighted averages were 0.54 ± 0.14 g and 1.39 ± 0.20 g for the pristine and pre-treated foams, respectively. Hence, it was demonstrated that PU foams with the pre-treatment can retain more water. To complete the pre-treatment, the sponges were rinsed many times with Millipore water and dried under vacuum for 12 h at 80 °C.

The incorporation of TiO_2 nanostructures into PU was carried out by manually dipping the PU foams into the previously mixed solution (solution A + B). The immersion time was 5 s and a sequence of 5 dipping cycles was performed at RT (see step 3 in Fig. 2). Some bubbles were formed after each dip and to remove them, foams were squeezed several times with tweezers. A hairdryer was then used to dry the foams (the height of the foams was 22 cm and the distance between the hairdryer and the foam was around 7 cm). Between each dipping cycle, foams were dried for 10 min,[65] Fig. 2. Lastly, they were ultrasonically cleaned for 1 h to remove unbonded particles and dried at 80 °C overnight under vacuum in a desiccator. The same foam was weighed before the TiO_2 impregnation (~0.066 g), after the TiO_2 impregnation (~0.071 g) and after the ultrasonic cleaning (~0.069 g). The final weight of the TiO_2 nanopowder on the foam substrate was around 3 mg and it
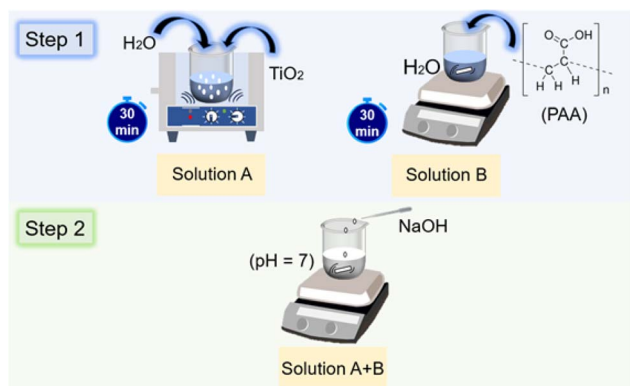

Fig. 1 Diagram illustrating the process of preparing the dip-coating solution for the impregnation of PU foams with TiO$_2$ nanostructures. Steps 1 and 2 illustrate the preparation of solutions A, B and A + B, respectively.

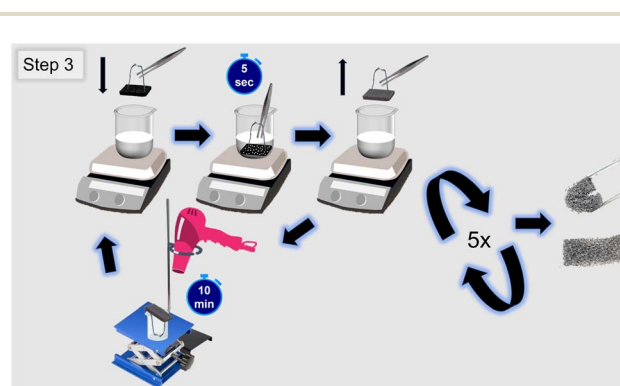**Fig. 2** Diagram illustrating the dip-coating procedure. Step 3 represents the dip-coating and drying processes to obtain TiO$_2$-PU foams. Real photographic images of the produced TiO$_2$-PU foam are also visible.

maintained the same initial dimensions. Macrographs of the TiO$_2$-PU foam are visible in Fig. 2, in which one of them shows that its flexibility is maintained after the impregnation and drying procedures. The technique employed proved to be simple and replicable.

Characterization techniques

XRD measurements of the nanopowders were conducted with an Aeris Benchtop XRD System equipped with a PIXcel1D detector. The XRD diffractograms were acquired from 10° to 90° (2θ) considering a step of 0.02°. The TiO$_2$ brookite, rutile and anatase simulated diffractograms were obtained from the Crystal Structure Database (ICSD) with file numbers 36408, 9161 and 9852, respectively.

SEM images were acquired with a Regulus 8220 Scanning Electron Microscope from Hitachi. The microscope has an EDS from Oxford Instruments.

STEM and transmission electron microscopy (TEM) images were obtained with an HF5000 microscope from Hitachi operated at 200 kV. High-angle annular dark-field (HAADF) imaging, This is a probe-corrected cold field emission gun (FEG) instrument equipped with an EDS detector (100 mm^2) also from Oxford Instruments. The sonicated dispersion containing the nanopowders was directly dropped onto lacey-carbon copper grids and permitted to air-dry prior to observation. STEM observations allowed the determination of the average particle size and standard deviation, estimated by measuring 40 nanostructures.[66]

The determination of the specific surface area was achieved by nitrogen adsorption according to the BET method, in the determined p/p_0 range and following the methodology described in ISO-9277.[67] The results were obtained at 77 K using the ASAP 2010 Micromeritics adsorption equipment. Before the experiments, an outgassed procedure was carried out overnight (at 120 °C, under vacuum) for the TiO$_2$ nanopowders ($\sim$0.2 g).

The XPS experiments were performed using a Kratos Axis Supra with monochromatic Al Kα irradiation (1486.6 eV). The XPS scans were acquired using a 225 W X-ray power and 40 eV of pass energy. The peaks were adjusted to C 1s at 284.8 eV. The XPS data were analysed using the CasaXPS software.

RT PL and PL excitation (PLE) experiments were conducted for all TiO$_2$ nanopowders. A Fluorolog-3 setup from Horiba Scientific was used with a double additive grating Gemini 180 monochromator (1200 g mm^{-1} and 2 × 180 mm) in the excitation and a triple grating iHR550 spectrometer in the emission (1200 g mm^{-1} and 550 mm). The excitation source used was a 450 W Xe lamp, exploring different excitation wavelengths. The PLE experiments were carried out by monitoring the observed emission maximum.

Characterization of TiO$_2$ nanopowders: adsorption and photocatalytic degradation of tetracycline under simulated solar light

Tetracycline standard curves were obtained from RT UV-vis absorption spectra with various concentrations of 5, 10, 15, 20 and 30 ppm. The linear expression that relates TC

concentration and absorbance can thus be obtained (Fig. S1†). The photocatalytic experiments followed the ISO-10678.[68] 25 mg of each nanopowder (TiO$_2$_EtOH, TiO$_2$_IPA and TiO$_2$_H$_2$O) was stirred at 120 rpm with the pollutant's solution (50 mL of the tetracycline solution ($\sim$30 ppm)) and kept in the dark for 240 min (4 h) to establish the adsorption–desorption equilibrium. Afterwards, 3 mL of aliquots were collected and the decay of the maximum absorption peak of tetracycline (at $\lambda = 360$ nm (ref. 69)) was analyzed using a spectrophotometer at fixed time intervals in the 200–450 nm range. The adsorption mechanisms were studied by using five kinetic models: first-order, the McKay and Ho pseudo-second order, Weber–Morris intraparticle diffusion, Elovich, Bangham and Boyd.[70,71] The respective equations (eqn (S4)–(S11)†) are depicted in the ESI file.†

After the adsorption experiments, the photocatalytic activity of the TiO$_2$ nanopowders was evaluated considering the degradation of tetracycline from Sigma-Aldrich. The photocatalytic experiments were also conducted at RT and in triplicate ($n = 3$) for the TiO$_2$ nanopowders, as can be seen by the error bars included (before and after light exposure).

A blank experiment was also carried out without the catalysts and under solar light. The solar light experiments were performed by using a light-emitting diode (LED) solar simulator LSH 7320 (AM 1.5 spectrum) with an output of 100 mW cm^{-2} (equivalent to 1 sun). The photocatalytic performance of the TiO$_2$ nanopowders was evaluated by recording the spectra on a UV-vis spectrophotometer at various times, up to a complete duration of 0.5 h (30 min). For the reusability tests, after the first cycle, the catalyst that exhibited the best performance was recovered from the solution by centrifugation at 6000 rpm for 5 min. The solution was discarded and the nanopowder was dried at 60 °C overnight under vacuum. The dried nanopowder was then tested under identical experimental conditions with the volume of TC solution adjusted to match the amount of available material. The pH of the solution remained unchanged.

For the regeneration and reutilization experiments, 40 mg of the recovered catalyst (obtained by centrifugation after the first photocatalytic cycle) was dispersed in 150 mL of deionized water and exposed to UV light. The UV system (model HNSL from Osram Puritec) is composed of three mercury lamps of 95 W each. The total light intensity is 35 mW cm^{-2}. The solution vessel was positioned 27.5 cm away from the UV light source for 240 min. Subsequently, the TiO$_2$ nanopowder was separated by centrifugation, washed with deionized water and dried under vacuum overnight. The dried material was used as the catalyst in the following catalytic cycle for adsorption and photocatalytic degradation of TC under the solar simulator.[72]

The species and mechanisms involved in the photocatalytic degradation process of TC over the TiO$_2$_EtOH nanopowder under simulated solar irradiation were explored by using reactive oxygen species (ROS) scavengers. In these assays, EDTA was used as a hole (h$^+$) scavenger, H$_2$O$_2$ as an electron scavenger (e$^-$), IPA as a hydroxyl radical ($^{\bullet}$OH) scavenger, BQ as the superoxide radical ($^{\bullet}$O$_2^-$) scavenger and sodium azide as a singlet oxygen (^{1}O$_2$) scavenger.[73]

The trapping experiments were carried out using identical conditions to those employed to assess both adsorption and

718 | Environ. Sci.: Adv., 2025, 4, 713–738

© 2025 The Author(s). Published by the Royal Society of Chemistry

photocatalytic performance. Before the trapping experiments, 5 mL of a 0.5 mM aqueous solution of each scavenger was added to 50 mL of TC solution containing 25 mg of the TiO_2 nanopowder.[32,74] The time of the solution in the dark and under light irradiation was kept fixed for 240 min and 30 min, respectively. For comparison, a solution without a scavenger, but with a photocatalyst and 5 mL of deionized water was also exposed to light.[32,74]

Characterization of TiO_2 PU foams: photocatalytic degradation of tetracycline under simulated solar light

The photocatalytic activity of the TiO_2_EtOH nanostructures on PU foams was also evaluated for the degradation of tetracycline. Each TiO_2 PU foam is added to 15 mL of tetracycline solution and the experiments are conducted in the dark for 1 h to achieve the absorption–desorption equilibrium and under simulated solar light for 180 min. For the reusability tests, in this case, no centrifugation was required prior to the measurements in the spectrophotometer. The functionalized TiO_2 PU foam was only washed with deionized water prior to the following cycle.

Ecotoxicity assays

Artemia salina or brine shrimp is a zooplankton used to feed larval fish.[75-77] This organism is reported to be a suitable test organism for toxicity studies in the presence of nanostructures.[75,76] For this reason, it was selected as a biological safety model test. Acute toxicities of PU foams with and without TiO_2 nanostructures on *A. salina* were investigated.

To prepare Artemia's environment, artificial seawater was first prepared by mixing regular tap water with commercial seawater salt, according to supplier instructions. Then, dry *A. salina* cysts were added to the artificial seawater and were left to hatch under aeration and artificial light, for 48 h, at 25–30 °C. Afterwards, 900 μL of artificial seawater, containing 10 to 15 nauplii, pristine PU foams and pre-treated TiO_2 PU-foams with dimensions of $1.5 \times 1.5 \times 1.5$ cm³; 10% DMSO as positive control; and artificial seawater as negative control were added to 24-well plates and incubated for 24 h, at 25–30 °C. After that, the dead nauplii were counted. To kill the remaining nauplii, 100% DMSO was added to all the wells and left to incubate for 2 h, at 25–30 °C.[78,79] After counting the total *A. salina*, the mortality (%) was calculated according to eqn (1).

$$\text{Mortality}(\%) = \frac{\text{Dead}_{24\text{ h}}}{\text{Dead}_{\text{Total}}} \times 100 \tag{1}$$

$\text{Dead}_{24\text{ h}}$ represents the number of dead *A. salina* nauplii 24 h after incubation and $\text{Dead}_{\text{Total}}$ represents the total of nauplii present in each well test. PU foams were tested with five replicates.

Results and discussion

Structural characterization of the TiO_2 nanopowders

XRD. The X-ray diffractograms of the TiO_2 nanopowders (TiO_2_EtOH, TiO_2_IPA and TiO_2_H_2O) are shown in Fig. 3. In the presence of ethanol, all experimental diffraction maxima
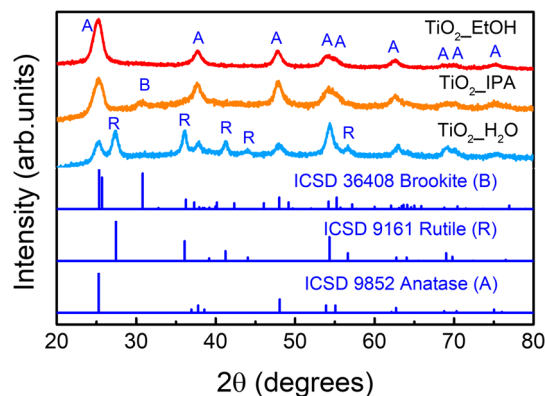

Fig. 3 X-ray diffractograms of the TiO_2 nanopowders (TiO_2_EtOH, TiO_2_IPA and TiO_2_H_2O) synthesized under microwave irradiation at 200 °C for 10 min. The simulations of TiO_2 brookite (ICSD 36408), rutile (ICSD 9161) and anatase (ICSD 9852) are also presented for comparison.

can be assigned to the tetragonal TiO_2 anatase crystalline phase (ICSD 9852). An analogous study reported the production of TiO_2 nanostructures by microwave irradiation in ethanol under similar conditions of time and temperature, *i.e.*, 10 min and 200 °C. In this study, the XRD also showed a pure TiO_2 anatase phase.[39] However, when isopropanol was used, besides observing the anatase diffraction maxima, another diffraction maximum appears at around 30° (2θ), ascribed to the (121) plane of the orthorhombic brookite crystalline phase (ICSD 36408). Despite the experimental difficulties in obtaining pure brookite, previous studies have shown that this phase can appear as a secondary phase in acidic alcohol-based solutions under optimum conditions of acidity, temperature and precursor concentration.[80-82] For the TiO_2_H_2O nanopowder, a clear mixture of rutile (ICSD 9161) and anatase crystalline phases is identified. This result is in accordance with previous reports on TiO_2 synthesis in an acidic medium by a microwave-assisted hydrothermal synthesis at 200 °C for 10 min, in which the formation of both anatase and rutile was observed.[83]

Electron microscopy

Scanning electron microscopy. The effect of different solvents on TiO_2 nanomaterials was investigated using scanning electron microscopy. From Fig. 4(a and b), the formation of micro-sized TiO_2 aggregates can be seen. These aggregates tend to have a spherical shape; however, elongated aggregates were also observed. From Fig. 4(b) and its inset, it can be noted that these larger aggregates are composed of very fine nanocrystals. TiO_2 micrometer spherical aggregates were previously reported with ethanol as a solvent in microwave synthesis.[39,68] Moreover, it can also be inferred that these larger aggregates are highly porous (refer to the arrows/dark spots in the inset of Fig. 4(b)). When it comes to the TiO_2_IPA nanopowder (Fig. 4(c and d)), the formation of one-dimensional (1D) nanostructures can be detected, with other smaller nanocrystals with an undefined shape (refer to the inset in Fig. 4(d)). These very fine TiO_2 nanocrystals tend to aggregate;[84] however, no specific larger structure was found for this condition of synthesis. XRD
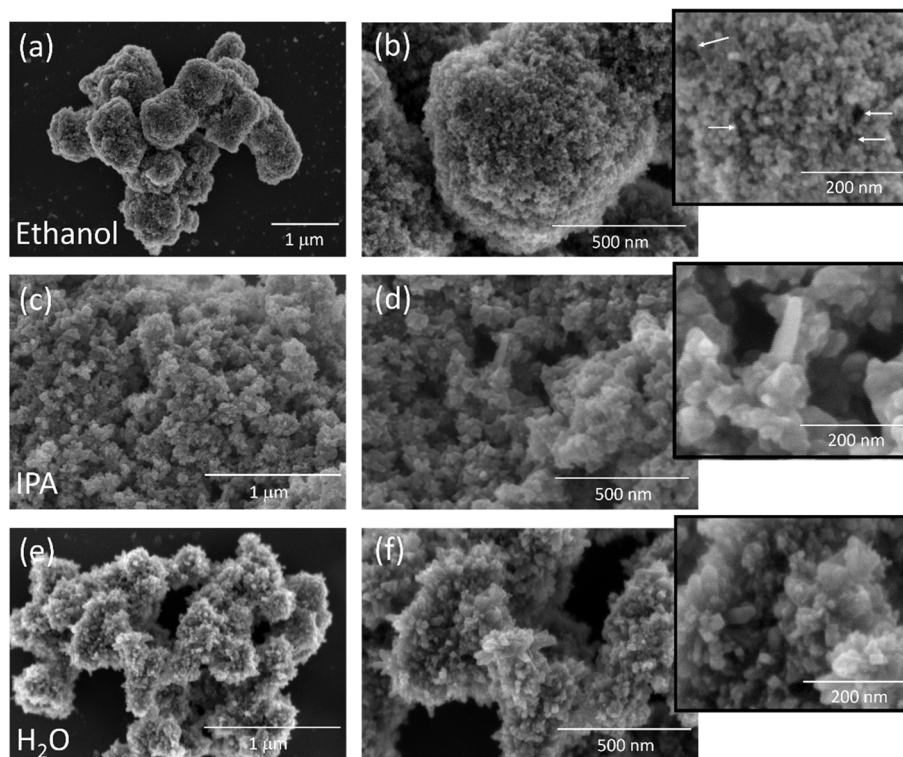
© 2025 The Author(s). Published by the Royal Society of Chemistry

Environ. Sci.: Adv., 2025, **4**, 713–738 | **719**

Fig. 4   SEM images of the TiO$_2$ nanomaterials, (a and b) TiO$_2$_EtOH, (c and d) TiO$_2$_IPA and (e and f) TiO$_2$_H$_2$O.

measurements determined that this nanomaterial was mostly composed of anatase with a minor presence of brookite, and for that reason, the heterogeneity observed in this nanomaterial can be related to the mixture of phases. As for the TiO$_2$_H$_2$O nanomaterial, the synthesis carried out in water resulted in 1D nanostructures. However, under this condition, it is clear that the TiO$_2$ nanorods presented a tetragonal shape, which has

been previously reported to be from the rutile phase.[85] This observation corroborates the XRD measurements, in which a mixture of rutile and anatase was identified. Nanocrystals with an undefined shape were also observed, but the 1D nanostructures dominated, as can be seen in Fig. 4(e and f) and the inset in Fig. 4(f). The nanocrystals synthesized with H$_2$O also tended to aggregate in larger structures, and in this case, the

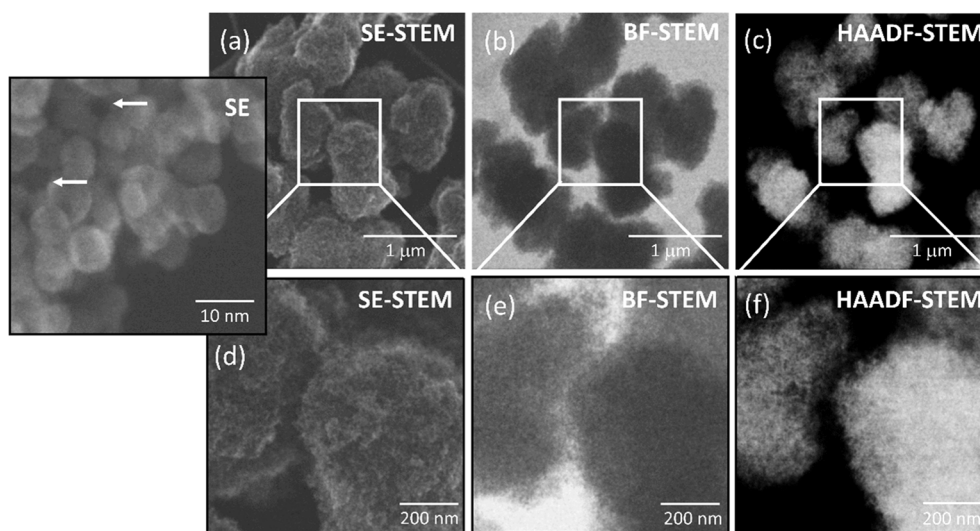Fig. 5   (a and d) SE-STEM, (b and e) BF-STEM, and (c and f) HAADF-STEM images of the micro-scaled TiO$_2$ aggregates of the TiO$_2$_EtOH nanomaterial highlighting their porous characteristics. The inset shows that the aggregates are composed of TiO$_2$ nanocrystals. The presence of spaces/voids is also evident between the nanocrystals (arrows) suggesting porosity at the nanoscale.

formation of quasi-spherical micro-sized aggregates can be observed.

Scanning transmission electron microscopy. The TiO₂_EtOH, TiO₂_IPA and TiO₂_H₂O nanostructures were also investigated using STEM analyses. In accordance with SEM images, the formation of micro-sized TiO₂ nanocrystal aggregates for the material synthesized with ethanol is clear. From the STEM images in Fig. 5, the presence of porosity is evident even at the nanoscale (arrows in the inset). As shown in the inset of Fig. 5 and S2,† faceted TiO₂ nanocrystals and others with round edges could also be observed. The average TiO₂ nanocrystals' size was found to be 5.93 ± 0.94 nm.

The TiO₂_EtOH nanocrystals were further investigated using atomic-resolution annular bright-field (ABF) and high-angle annular dark-field (HAADF) imaging (Fig. 6). The STEM secondary electron (SE) images were of great importance since the topographical contrast assisted the interpretation of the ABF and HAADF images.[86] The Ti atomic columns are visible in the ABF and HAADF images, albeit with reverse contrast.[87] The Ti atomic columns correspond to lattice spacings of 0.27 nm and 0.29 nm that perfectly match the (110) and (102) atomic planes of anatase, respectively. Fast Fourier transform (FFT) of lattice images acquired along the [221] zone axis showed that the angle between (1$\bar{1}$0) and (10$\bar{2}$) is ~56°, in accordance with the theoretical value reported for pure crystalline TiO₂ anatase

(ICSD 9852). The TiO₂ nanocrystals show structural defects in the STEM images, attested by a darker topographical contrast in the SE images (arrows pointing to the absence of Ti atoms). Surface steps can also be observed in Fig. 6(e and f). The TiO₂ faceted nanocrystal was further investigated (Fig. 6(h and i)) and high-index {012} and {102} facets can clearly be observed. TiO₂ anatase high-index nanocrystals have been reported to display high photocatalytic activities when compared to low-index faceted crystals due to their unique atomic and electronic structure, with a high density of atomic steps, kinks, ledges, dangling bonds and abundant unsaturated coordination sites.[88] It has been proposed that higher index planes containing structural steps cause the electrons to be trapped at the low-coordinated Ti cations at the steps, thereby enhancing the separation of charges. Consequently, these additional electrons contribute to surface processes. On the other hand, the trapping of holes at the surfaces of anatase is facet-dependent. Studies have shown that the (001) and (100), and the (105) and (107) surfaces have the strongest affinity to trap holes, favoring the charge separation on anatase crystals and allowing the presence of holes on these surfaces to interact with molecular adsorbates. It has been suggested that hole trapping mainly occurs within the subsurface layers rather than on the surface facets for the (101), (110), (112) and (103) surfaces. This could potentially extend the lifetime of electrons, preventing recombination.[89] In
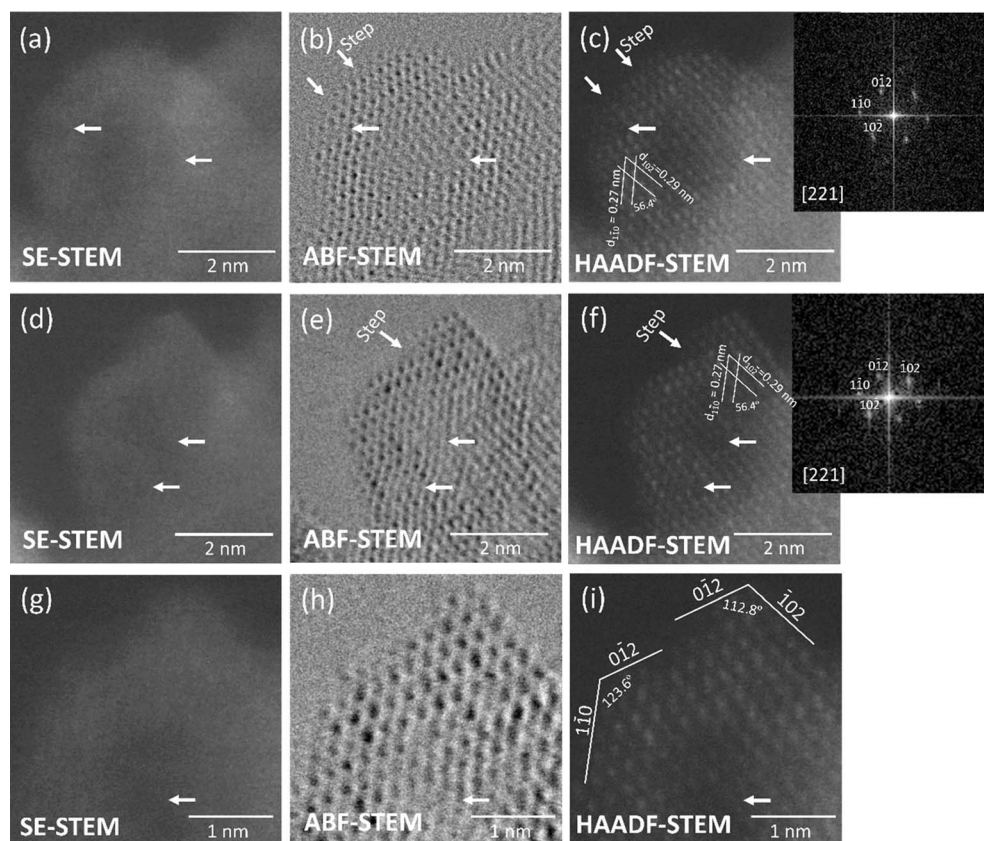
Fig. 6 (a) SE-STEM, (b) ABF-STEM and (c) HAADF-STEM images acquired simultaneously of a TiO₂ anatase nanocrystal of the TiO₂_EtOH nanomaterial. The inset shows the FFT image obtained from (c). (d) SE-STEM, (e) ABF-STEM and (f) HAADF-STEM images of a TiO₂ faceted nanocrystal with a FFT image of (f) presented in the inset. The facet nanocrystal of images (d–f) was further magnified in (g–i). The arrows point to the atomic-level surface structural defects.

the case of the (102) facets of anatase, the presence of surface defects was demonstrated with terminations of oxygen completely distinct from the predicted stoichiometric structures.[90] Low-index faceted anatase nanocrystals were also observed in the TiO2_EtOH nanomaterial (Fig. S2†); however, no topographical contrast was detected in the SE images or the ABF and HAADF images of these nanocrystals, suggesting that they are defect-free. To the authors' knowledge, for the first time, TiO2 anatase faceted nanocrystals with sizes in the order of ~6 nm had their atomic structure investigated using STEM experiments to determine the nanocrystals' surfaces and presence of structural defects, including steps on their high-index {012} facets and absence of Ti atoms in the bulk (see arrows in Fig. 6(b, c, e and f)). Previously, only larger TiO2 anatase defective crystals like sub-micrometer rods were reported.[90] The STEM experiments in this study determined that microwave synthesis with ethanol as the solvent resulted in low- and high-index faceted anatase nanocrystals, the latter with surface structural defects, that when associated with the porous structure of the micro-sized aggregates, effectively play a key role in the photocatalytic activity of these materials.

The TiO2_IPA nanomaterial was also studied using atomic-resolution STEM (Fig. 7), and in accordance with the SEM observations, the nanomaterial is composed of 1D nanostructures and nanoparticles with undefined shapes. XRD analysis demonstrated that this material is mainly based on the TiO2 anatase phase with a minor presence of brookite. This mixture of phases was confirmed using the electron diffraction pattern in the inset of Fig. 7(d). The presence of TiO2 nanorods is evident in the STEM images (Fig. 7(a–c)) and in the BF-TEM image (Fig. 7(d)), in which 1D nanorods with different sizes are perceptible. The larger nanorods with ~200 nm in length were in minority, while the majority of nanorods appear with 28.5 ± 4.3 nm in length and width, respectively. One of the larger TiO2 nanorods was individually investigated (Fig. 7), and from the atomic-resolution

STEM images and the FFT patterns, it can be concluded that the nanorods had the tetragonal TiO2 anatase phase (Fig. 7(f)). Moreover, the nanorod grew along its c axis in the [100] direction, suggesting a fast growth rate along this direction. From Fig. 7(e and f), it can be observed that Ti atomic columns are perpendicular to each other. A lattice spacing of 0.19 nm perfectly matches the (200) and (020) atomic planes of anatase.[91] When observed along the [00$\bar{1}$] zone axis, it is evident that the angle between (200) and (020) is 90°, in accordance with anatase (ICSD 9852). The facets of the nanorod are {010} surfaces. The surface energy of the major facets of anatase follows the order {001} (0.90 J m^{-2}) > {010}/{100} (0.53 J m^{-2}) > {101} (0.44 J m^{-2}).[88] The relatively high surface energies of the {001} and {100}/{010} facets are ascribed to the 100% five-fold coordinated titanium atoms (Ti$_{5c}$), in contrast to the 50% Ti$_{5c}$ found on {101} facets.[92] The {101} facets of anatase have been extensively investigated; however, it has been reported that the {010}/{100} facets display higher reactivity than {101} ones due to the higher concentration of low-coordination Ti$_{5c}$ centers making crystals with these high-energy facets desirable for photocatalysis.[92,93] When it comes to surface energy, it has been reported that high-index facets display higher surface energy. The surface energy associated with the {012}/{102} facets is unknown, as far as we know, and cannot be easily measured in the present case, due to the mixed nanocrystal types. However, the {201} facets, with a surface energy of 1.72 J m^{-2} have been described to have more uncoordinated Ti atoms, promoting the photogeneration of hydroxyl radicals.[88] The {102} and {103} surfaces have undersaturated Ti atoms and high-density step defects, resulting in high photocatalytic activity.[94] The surface energy and atomic structure of crystals are vital for the photocatalytic performance of TiO2 anatase[88] and the literature suggests that high-index facets have better photocatalytic behavior.

Fig. 8 shows STEM images of the TiO2_H2O nanomaterial. XRD analysis showed that the TiO2 nanostructures are a mixture of TiO2 rutile and anatase with the presence of tetragonal-
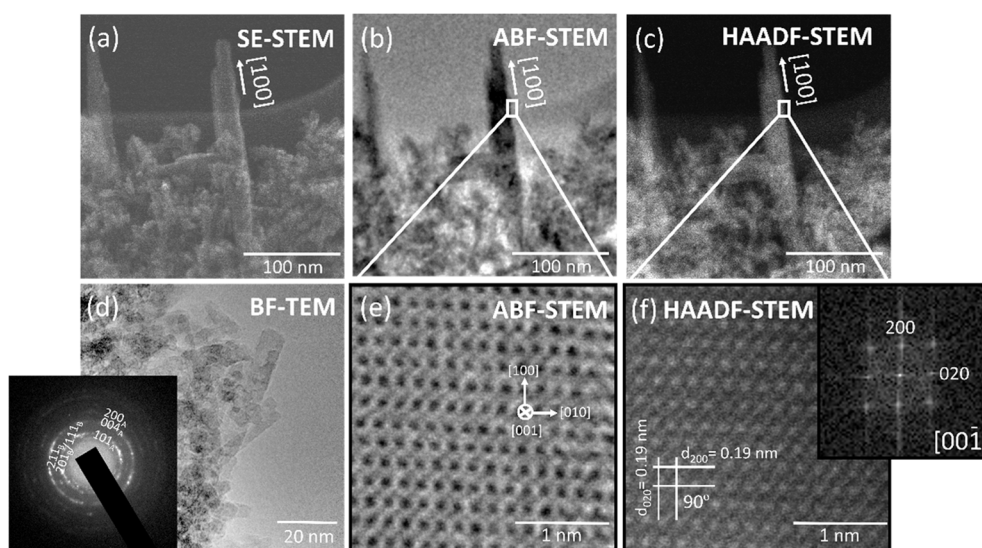
Fig. 7 (a) SE-STEM, (b) ABF-STEM, (c) HAADF-STEM and (d) BF-TEM images of TiO2_ IPA nanocrystals. The inset in (d) depicts the electron diffraction pattern of TiO2 nanocrystals with the anatase (A) and brookite (B) phases. Atomic-resolution (e) ABF-STEM and (f) HAADF-STEM images of an individual TiO2 nanorod (~200 nm). The inset in (f) shows the FFT image of the area in (f).

722 | *Environ. Sci.: Adv.*, 2025, **4**, 713–738

© 2025 The Author(s). Published by the Royal Society of Chemistry

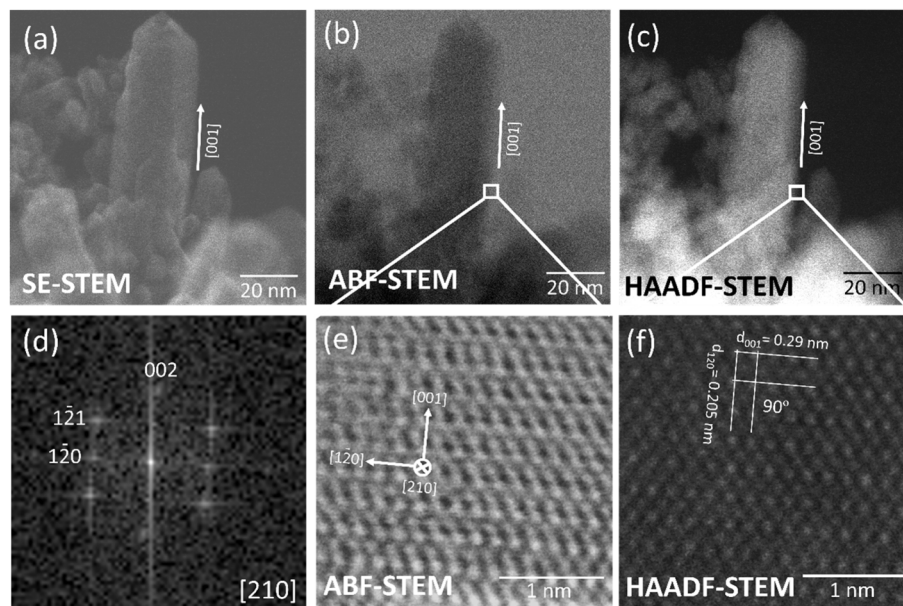Fig. 8 (a) SE–STEM, (b) ABF–STEM and (c) HAADF–STEM images of TiO_2_ H_2O nanocrystals. An individual TiO_2 nanorod was magnified and in (d) the FFT image of the area observed in (e and f) is presented. (e) Atomic-resolution ABF–STEM and (f) HAADF–STEM images of the nanorod analyzed.

shaped nanorods, attributed to the rutile, as confirmed by SEM (Fig. 8(e and f)). STEM observations corroborated the SEM images, in which the nanostructures are mostly nanorods, with other nanocrystals having an undefined (quasi-spherical) shape. The rutile tetragonal nanorods have a pencil-like tip shape, and the presence of structural defects on the nanorod tip and throughout its length was detected. An individual nanorod (~100 nm) was further investigated (Fig. 8), and based on the atomic-resolution STEM images and the FFT pattern, it can be proven that the nanorods correspond to the tetragonal rutile (Fig. 8(d–f)). The axis direction of the nanorod is [001]. The crystal growth along the c-axis has been associated with the fastest growth rate.[95] A lattice spacing of 0.2959 nm has been ascribed to the (001) atomic planes of rutile,[96] while the reported 0.2054 nm matches the (120) rutile atomic planes, as seen in Fig. 8(f). Along the [210] zone axis, the angle between (001) and (120) is 90°, in accordance with the tetragonal rutile structure (ICSD 9161). Moreover, photocatalysts based on a mixture of rutile and anatase have been largely investigated for their high photocatalytic activity.[97–99]

Specific surface area. The BET specific surface area of the TiO_2 nanopowders synthesized with different solvents is presented in Table 2.

Table 2 BET specific surface area of the TiO_2_EtOH, TiO_2_IPA and TiO_2_H_2O nanopowders synthesized under microwave irradiation at 200 °C for 10 min

TiO_2 nanopowders	Specific surface area ($m^2\ g^{-1}$)
TiO_2_EtOH	231
TiO_2_IPA	177
TiO_2_H_2O	121

As seen in Table 2, the highest specific surface area was obtained with TiO_2_EtOH followed by TiO_2_IPA and then TiO_2_H_2O. Several solvents led to TiO_2 nanostructures with various morphologies and, consequently, different specific surface area values were obtained. Moreover, intraparticle pores were observed in the $TiO2$_EtOH nanopowder aggregates by SEM and STEM analyses. Hence, the high density of pores is likely to have a significant influence on the specific surface area value. A larger surface area provides more available sites on the particle surface for the adsorption of pollutant molecules, which in turn enhances the photocatalytic process.[100] Although large aggregates were formed when ethanol was used as a solvent, these aggregates were composed of very small TiO_2 nanocrystals (average size of 5.93 nm), see the inset of Fig. 4(b). Therefore, not only the shape of the particles but also their size is likely to have contributed to the differences observed in Table 2. It should also be noted that compared with previous studies,[38,39,101] all the microwave-synthesized TiO_2 nanopowders exhibited much higher specific surface area values.

XPS. To study the surface properties of the TiO_2 nanopowders, XPS measurements were conducted. The survey spectra (Fig. S3†) show that all synthesized TiO_2 nanopowders are composed of titanium, oxygen and carbon (related to the adventitious carbon[102]). The high-resolution XPS spectra of Ti 2p and O 1s (deconvoluted) are visible in Fig. 9. As seen in Fig. 9(a), for all synthesized TiO_2 nanopowders, the Ti 2p core level shows two components: Ti $2p_{1/2}$ and Ti $2p_{3/2}$, which are located at 458.6 eV and 458.6 eV and are both associated with Ti^{4+} oxidation state.[103,104] The Ti 2p peak shapes are identical for all TiO_2 nanopowders and no peak shift could be identified. Regarding O 1s spectra, the deconvolution was fitted with three components according to the literature,[105] see Fig. 9(b). The first component at 529.7 eV corresponds to lattice oxygen atoms
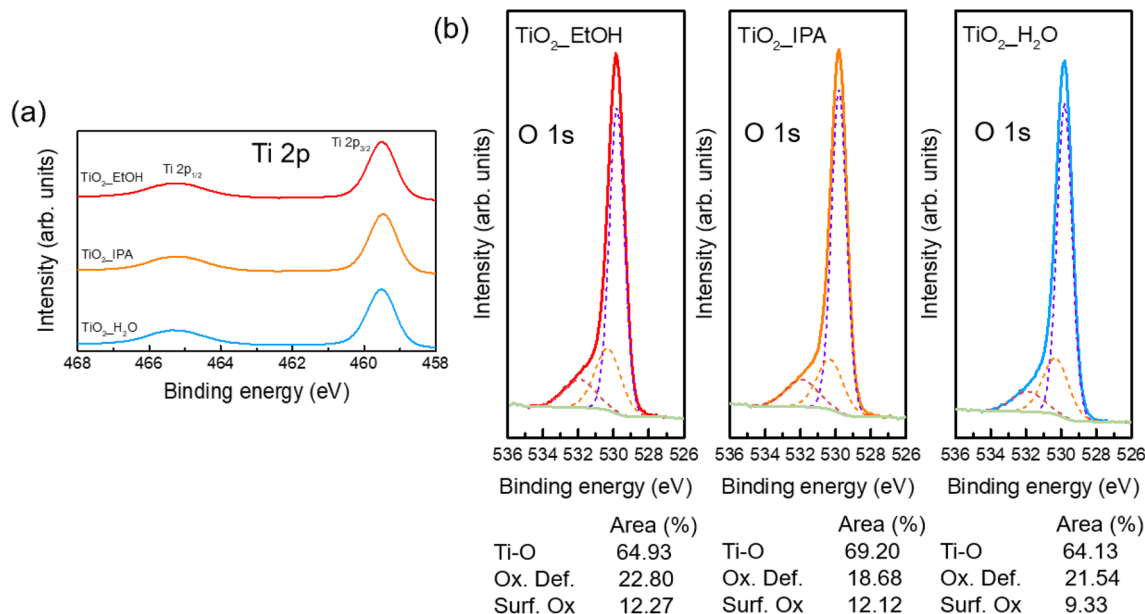
Fig. 9 (a) XPS high-resolution Ti 2p spectra of the TiO$_2$_EtOH, TiO$_2$_IPA and TiO$_2$_H$_2$O nanopowders. (b) XPS high-resolution O 1s spectra of the TiO$_2$_EtOH, TiO$_2$_IPA and TiO$_2$_H$_2$O nanopowders. The peak area of each component (lattice oxygen (Ti–O), oxygen-deficient regions and surface oxygen) is also shown for each synthesis condition.

(O^{2-}) in a fully coordinated TiO$_2$ with the Ti^{4+} ions mainly from the bulk, the second component at 530.2 eV is usually assigned to oxygen-deficient regions (O$^-$, O^{2-}) of the metal oxide and the third component at 531.8 eV is related to surface oxygen, associated with the loosely adsorbed, dissociated oxygen or OH species from O$_2$ or H$_2$O on the surface of TiO$_2$.[106,107] These peak positions have been kept fixed during the fitting. Initially, the full-width half maxima (FWHM) have been left free to adjust (within ±0.1 eV). For the final fitting, an average FWHM was calculated for all components, which was then held constant between each nanopowder. Through the fitting, a clear decrease in surface oxygen was revealed for the TiO$_2$_H$_2$O nanopowder, compared to the ones synthesized with alcohol. This difference can be further visualized by plotting the normalized intensity of all O 1s emissions (Fig. S4†). This is also supported by the peak areas of the surface oxygen component (see Fig. 9(b)), in which a decrease in the peak area percentages was observed from around 12% for the TiO$_2$_EtOH and TiO$_2$_IPA nanopowders to 9% for the TiO$_2$_H$_2$O nanopowder. This suggests a higher adsorption of oxygen species by the TiO$_2$ nanopowders synthesized with alcohol, rather than water. As observed previously with the obtained specific surface areas and STEM analysis, the higher porosity and density of structural defects present at the high-index facets of TiO$_2$ anatase (surface and bulk structural defects) should be the major factors in the enhancement of capacity for surface oxygen adsorption.[106,107]

Optical characterization of the TiO$_2$ nanopowders

Photoluminescence measurements. Fig. 10 displays the PLE and PL spectra obtained for all synthesized TiO$_2$ nanopowders at RT. The PL spectra were obtained by exciting the nanopowders with 390 nm photons of an Xe lamp. As can be seen,

the spectra are dominated by a broad visible band peaked in the yellow-orange spectral region. The maxima of the PL bands are slightly different depending on the solvent used. The TiO$_2$_EtOH nanomaterial exhibits its maximum at ∼576 nm (∼2.15 eV), while the TiO$_2$_IPA and TiO$_2$_H$_2$O nanomaterials display maxima at ∼565 nm (∼2.19 eV) and ∼584 nm (2.12 eV), respectively. Besides, the TiO$_2$_EtOH nanomaterial evidences a higher PL intensity, ∼2.7 times higher than the one recorded for IPA, suggesting a lower contribution from nonradiative processes when compared to the remaining nanopowders and/or a higher contribution from the defect centres that give rise to the observed luminescence. It is also worth noting that the
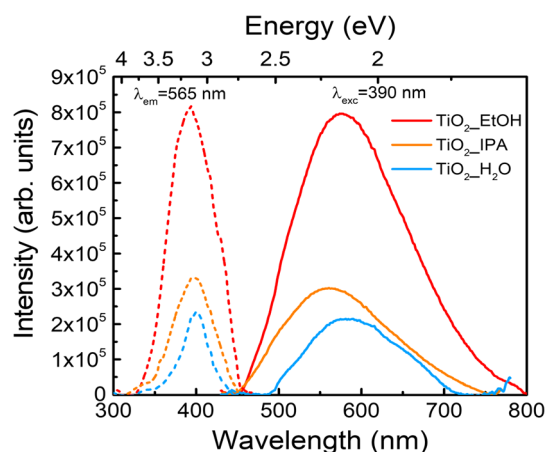

Fig. 10 RT PLE/PL spectra (represented by dashed lines and solid lines, respectively) of the TiO$_2$_EtOH, TiO$_2$_IPA and TiO$_2$_H$_2$O nanopowders. PL was acquired under the 390 nm excitation of an Xe lamp, while the PLE spectra were obtained by monitoring at the maxima of the PL bands.

quantity of powder analyzed was similar for all experiments and that all excitation and light collection conditions were kept constant during the experiments to enable a reliable comparison of the absolute intensities of the PL emission.

Broad yellow/orange bands have been previously reported in the literature for TiO_2 anatase.[108–112] According to Iijima et al.,[112] the band that appears at ∼2.1 eV is likely related to the presence of oxygen vacancies at the particle's surface, since these authors observed that its contribution decreases with increasing annealing in a flowing oxygen atmosphere. It has also been considered that the broad band observed was composed of more than one component overlapped. Indeed, the large FWHM observed for the present nanopowders should also consider this possibility. Another common band present in this spectral region for anatase crystals is the one centered around 2.3–2.5 eV,[111,112] which is often attributed to the radiative recombination of self-trapped excitons (STE) localized in TiO_6 octahedra, and which the mentioned authors claimed to be independent of the annealing process.[112] Tang et al.[113] analyzed the PL properties of TiO_2 anatase single crystals and argued that the luminescence observed in this region was due to self-trapped excitons and/or impurity-trapped excitons, in line with what is often reported in several titanates containing TiO_6 octahedra.[113] Nevertheless, the peak position and spectral shape of this band are seen to be strongly dependent on the surrounding environment and the excitation conditions, which suggests the overlap with other possible contributions.[111] The presence of other recombination processes involving surface states and trap states has been identified as potential contributors to the broad PL band observed in anatase crystals in this spectral region, which becomes more relevant as the specific surface area of the particles increases.[111]

In fact, when one considers the PLE spectra, a broad excitation band is observed in all cases, particularly for the TiO_2_EtOH and TiO_2_IPA nanopowders. In both cases, the bands have a peak at ∼395 nm (∼3.15 eV), likely corresponding to their optical bandgap energies. These results indicate that the emission bands are preferentially populated *via* photons with energies equal to the bandgap one, with an important contribution from shallow sub/below bandgap states, likely related to defect states, as mentioned above. For the TiO_2_H_2O nanopowder, the excitation band maximum was found to be at ∼401 nm (∼3.09 eV), at a slightly lower peak position than the one identified for the other two nanopowders. Indeed, this nanopowder was shown to be composed of both rutile and anatase phases and rutile is known to have a lower bandgap energy than that of anatase (∼3.0 eV *vs.* ∼3.2 eV (ref. 114)); hence, the observed PLE band may correspond to an overlap of both contributions.

Adsorption kinetics study of the TiO_2 nanopowders. To understand the effectiveness of pollutant molecule uptake from the solution by the adsorbent, the adsorption kinetics was studied.[115] The influence of contact time on tetracycline adsorption capacity onto TiO_2 nanopowders is depicted in Fig. 11. The uptake of tetracycline molecules reaches its maximum value on average after 120 min for TiO_2_IPA, whereas for TiO_2_EtOH, 240 min are necessary to reach equilibrium. Since the adsorption

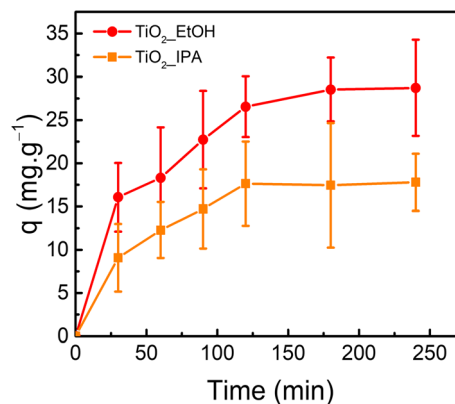Fig. 11 Influence of contact time on tetracycline adsorption capacity onto TiO_2 nanopowders. Experimental conditions: q_{max} is 34 mg g^{-1}, [tetracycline] ∼25–30 ppm, V = 50 mL, max. adsorption time = 240 min, $m_{adsorbent}$ = 25 mg. The error bars indicate the standard deviations of triplicate experiments (n = 3).

capacity of TiO_2_H_2O was almost null, it cannot be seen in Fig. 11. Fig. 11 shows that at the initial moments of the contact period, the adsorption is fast, especially with the TiO_2_EtOH nanopowder, and after that time it becomes slower near the equilibrium. A larger amount of vacant surface sites may be initially available for the adsorption to occur and then repulsive interactions between the solute molecules and the solid might take place.[116] In fact, the improvement of adsorption efficiency with the TiO_2_EtOH nanopowder compared with the other nanopowders might be related to its high specific surface area (Table 2), during the first 120 min (Fig. 11).

The average adsorption capacities of the TiO_2 nanopowders decrease in the following order: TiO_2_EtOH (28.73 mg g^{-1}) > TiO_2_IPA (17.80 mg g^{-1}) > TiO_2_H_2O (∼0 mg g^{-1}). Since the sorption efficiencies of TiO_2_IPA and TiO_2_H_2O are too low (34.7% and 0% after 240 min (4 h)) compared with the sorption efficiency of ethanol (∼55%), see eqn (S2) and (S3),† the adsorption mechanisms of tetracycline with both IPA and water nanopowders were not further investigated.

The adsorption process comprises three distinct stages. Initially, solute species are transferred from the bulk solution into the outer surface of the adsorbent (film diffusion). Then, solute molecules migrate from the adsorbent outer surface to the pores of the adsorbent internal surface (intraparticle diffusion). The last step is the adsorptive attachment of the solute species onto the active sites on the inner and outer surfaces of the adsorbent. Since this step occurs very quickly, it is considered negligible as a rate-controlling step. Hence, the adsorption rate is primarily governed either by the outer diffusion, intraparticle diffusion or both.[117,118]

To explore the adsorption process of tetracycline on the TiO_2_EtOH nanopowder, several models were employed to fit the experimental data, including pseudo-first-order kinetic, pseudo-second-order kinetic, Elovich, intraparticle diffusion, Bangham and Boyd plot models.[71] Through linear regressions of the kinetic plots, the kinetic parameters for each model were

© 2025 The Author(s). Published by the Royal Society of Chemistry

Environ. Sci.: Adv., 2025, **4**, 713–738 | **725**

calculated and are listed in Tables S1 and S2.† For the calculations, only the first cycle of adsorption was considered.

The pseudo-first-order model characterizes the rate at the initial stage of adsorption, but cannot describe the entire adsorption process.[119] The pseudo-second-order kinetic model, on the other hand, presumes that chemisorption governs the adsorption mechanism, with the sorption capacity being proportional to the number of active sites occupied on the adsorbent.[120] Conversely, the Elovich model suggests that the active sites of the adsorbent have different activation energies for chemisorption, and so, the rate of solute adsorption decreases exponentially with the accumulation of adsorbed solute.[121,122]

Comparing the three models, the experimental data are more closely aligned with the pseudo-second-order model, showing higher correlation coefficient values ($R^2 = 0.98$). Additionally, the calculated q values (q_e^{calc}) from the pseudo-second-order model are a better approximation of the experimental q values (q_e^{exp}). Hence, the adsorption process is driven by chemisorption. Other studies have already reported a similar behavior by TiO_2 nanomaterials.[123,124]

Since the pseudo-second-order model cannot identify the diffusion mechanism and the possible rate-limiting step of the adsorption process, the intraparticle diffusion model was also analyzed.[117]

According to eqn (S5),† a linear relationship between q and $t^{1/2}$ indicates the involvement of intraparticle diffusion in the adsorption process. Furthermore, if a straight line intercepts the origin in the plot, intraparticle diffusion is the rate-controlling step.[118]

As visible in Fig. S5,† multi-stage mechanisms are present. The linear regression analysis of the data gives three different regions for the TiO_2_EtOH nanopowder. The three stages are likely related to external diffusion or film diffusion, gradual adsorption and equilibrium.[125] The absence of intercepts at the origin (value of the intercept C) in the linear plots of the second and third stages is likely attributed to variations in mass transfer rates from the initial to final adsorption stages.[126] This suggests that intraparticle diffusion may not be the only rate-limiting step, with film diffusion also influencing the adsorption process.[71]

Bangham's model was also investigated and the value of the obtained regression coefficient was not higher than 0.95. This corroborates the major contribution of film diffusion of tetracycline onto the nanopowder (Fig. S6†).[127]

To determine the rate-limiting step in the adsorption process of TC onto TiO_2_EtOH nanopowder, the Boyd model was employed.[71,118] Through the plot of B_t (Boyd parameter) versus time (t), if a straight line intercepts the origin, intraparticle diffusion governs the rate of the process. Otherwise, the adsorption process is governed by film diffusion or chemical reaction dominates the adsorption rate. Fig. S7† shows that even though the plot was linear, it did not intercept the origin. Therefore, film diffusion primarily controls the adsorption process.[128,129]

Photocatalytic degradation of tetracycline using TiO_2 nanopowders. The photocatalytic activity of the TiO_2 nanomaterials synthesized at 200 °C for 10 min with different solvents under microwave irradiation was evaluated through the degradation of tetracycline under simulated solar irradiation. Before light exposure, the solutions containing tetracycline and the photocatalysts were stirred in the dark for 240 min. After that time, the solutions were exposed to simulated solar light for 30 min.
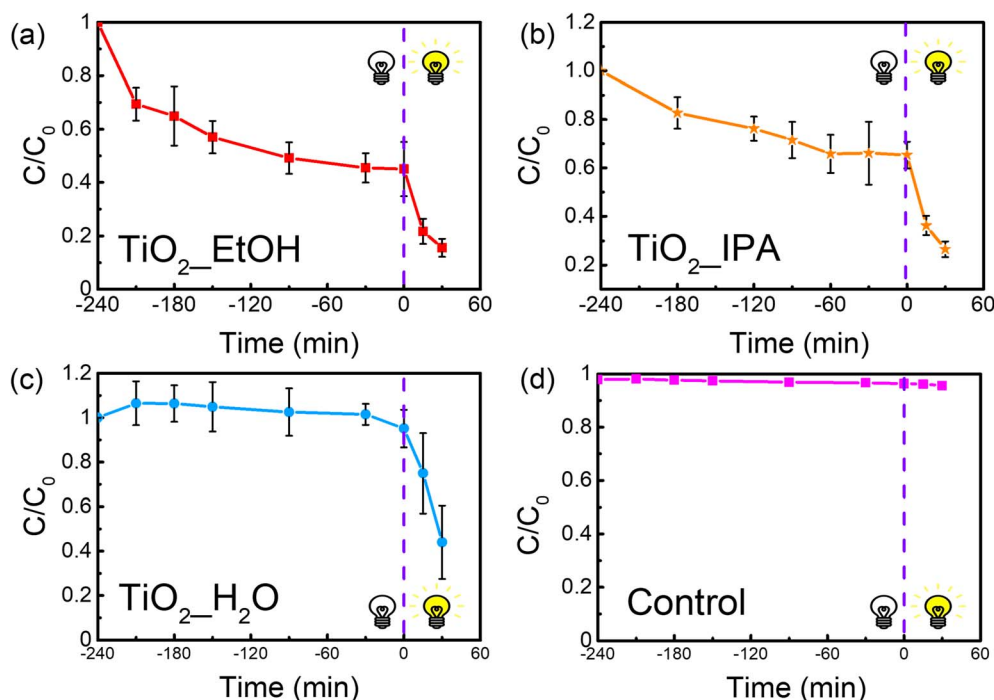
Fig. 12 Degradation profiles of tetracycline over TiO_2 catalysts (a) TiO_2_EtOH, (b) TiO_2_IPA, (c) TiO_2_H_2O and (d) without a photocatalyst, in the dark and under simulated solar light. Error bars indicate the standard deviations of triplicate experiments ($n = 3$) in (a–c).

726 | Environ. Sci.: Adv., 2025, **4**, 713–738

© 2025 The Author(s). Published by the Royal Society of Chemistry

During the blank experiments (photolysis), no degradation was observed, indicating that tetracycline does not degrade over time (Fig. 12). As previously discussed, the TiO$_2$_EtOH and TiO$_2$_IPA nanopowders showed a significant TC adsorption percentage after the dark (about 58% and 30% during the first cycle, respectively, see Fig. S8†), whereas with the TiO$_2$_H$_2$O there was no adsorption. However, after the time in the dark, under 30 min of solar light exposure and for all nanopowders, a clear decrease in C/C_0 is observed (Fig. 12). Moreover, the total TC removal percentages reach around 88%, 77% and 72% with the TiO$_2$_EtOH, TiO$_2$_IPA and TiO$_2$_H$_2$O nanopowders (Fig. 12), respectively.

The photocatalytic performance is highly influenced by the crystalline phase, particle morphology, crystallite size, specific surface area and crystal facets of the photocatalyst.[130] In terms of crystalline phases, mixtures of anatase/brookite, anatase/rutile, and pure anatase phase were obtained, respectively for the nanopowders synthesized in IPA, H$_2$O and ethanol. Many reports state that a mixture of TiO$_2$ crystalline phases could lead to a synergistic effect that would improve the separation of photogenerated charges.[131,132] However, this was not verified in the present study, and the findings demonstrated that the nanopowder comprising pure TiO$_2$ anatase displayed better photocatalytic performance. As seen from SEM and STEM images, the TiO$_2$_EtOH powder presented micrometer spherical/elongated aggregates with faceted nanocrystals and displayed porosity even at the nanoscale. In the case of both TiO$_2$_IPA and TiO$_2$_H$_2$O, nanorods and some particles with undefined shapes were observed, and for the latter, these nanostructures aggregated in quasi-spherical micro-sized particles. The porous structure of TiO$_2$_EtOH suggested that this material would have a higher surface area, which was confirmed by the BET measurements. In heterogeneous catalysis, most reactions between the catalysts and reactants occur on the catalyst's surface, in a way that a large surface area will not only provide more active sites at the catalyst surface to produce radical species but also anchor the organic pollutant's molecules.[133] Indeed, a larger specific surface area was obtained with the TiO$_2$_EtOH nanopowder, which provided more adsorption sites, resulting in an enhancement of tetracycline molecules to adsorb onto the surface of TiO$_2$, as visible with the adsorption kinetics study. The combination of a high adsorption capacity, together with the ability to produce radical species contributed to enhancing the removal of the pollutant from water. In fact, XPS measurements attested the ability of both TiO$_2$_EtOH and TiO$_2$_IPA nanopowders to adsorb surface oxygen.

At the atomic level, differences were evident between the different solvents used. In the case of the TiO$_2$_EtOH nanopowder, faceted nanocrystals (∼6 nm) with atomic structural surface (steps) and bulk (absence of Ti atoms) defects were observed on the high-index facets. The atomic arrangement of titanium and oxygen on the anatase phase determines the different facets formed, dominating the TiO$_2$ surface chemistry.[88] It is known that the low-index (101) TiO$_2$ anatase surface is the most stable, followed by the (001) one. However, the (001) surface has a higher photocatalytic activity than the (101)

surface.[134] Therefore, the interest in high-index TiO$_2$ anatase surfaces has been increasing lately since these nanomaterials exhibit exceptional photocatalytic properties when compared to low-index ones. Indeed, it has been demonstrated that high-index TiO$_2$ nanomaterials exhibit better adsorption and photooxidation performance than the low-index {001}, {100} and {101} surfaces.[88] Moreover, generally, high-index facets exhibit high surface energy, resulting in a high reactivity.[88] TiO$_2$ high-index faceted nanocrystals ({012} and {102} facets) were observed through STEM, and thus, are expected to significantly impact the overall photocatalytic activity of the nanomaterial owing to the presence of structural defects. In fact, the surface defects observed in the high-index facets, and suggested by the photoluminescence results, can contribute to stabilize these high-index facets, and consequently, enhance the separation of photogenerated charges and ultimately aid to boost the photocatalytic performance.[89,135] It is noteworthy that most reports on the synthesis of high-index facets of TiO$_2$ highly depend on the use of toxic chemicals.[88] Unlike these studies, an environmentally benign approach is herein proposed.

Integrating high-index facets with defective TiO$_2$ nanocrystals is highly desirable to strengthen the response in the visible light region and limit the recombination of photogenerated carriers.[88] Regarding the defects in TiO$_2$, Kong *et al.*[136] discovered that adjusting the ratio of bulk defects to surface defects in TiO$_2$ nanocrystals can significantly boost the separation of photogenerated charge carriers and lastly improve the photocatalytic performance. Yet, establishing a direct correlation between surface/bulk defects and photocatalytic activity remains difficult, mainly due to their interaction with other factors that influence the photocatalytic performance, such as crystalline phases and exposed crystal facets.[137]

Nevertheless, when it comes to surface defects, various reasons are attributed to their improvement in the removal of pollutants. The first is related to changes in the surface properties of TiO$_2$, which could induce different adsorption/desorption capabilities of reactants, intermediates, or products. Another reason is the light absorption ability. Due to the existence of these surface or sub-surface defects, new intermediate levels could be created within the band gap of TiO$_2$, leading to enhanced capacity for visible light absorption. The third reason has to do with disorders at the surface that could turn into traps for electrons or holes, limit the recombination of photogenerated charge carriers and consequently increase the lifetime of charge carriers in the material.[138–140]

Therefore, the enhanced photocatalytic activity observed in the TiO$_2$_EtOH nanopowder can be ascribed to a synergistic effect of factors. These include its high surface area stemming from a porous structure at the micrometer scale, as well as nanometer and atomic level contributions, characterized by pores within the nanocrystals, and the exposure of high-index crystal facets with atomic bulk and surface defects. Additionally, the higher capacity for surface oxygen adsorption further contributes to this enhanced activity.

To quantitatively compare the decomposition efficiency under solar light, the experimental data were fitted according to

© 2025 The Author(s). Published by the Royal Society of Chemistry

Environ. Sci.: Adv., 2025, **4**, 713–738 | **727**

Table 3 Kinetic parameters (rate constants k_{ap} and linear regression coefficients R^2) for the tetracycline degradation under simulated solar light without a photocatalyst (control) and with TiO$_2$ nanopowders synthesized with ethanol, IPA and water[a]

	Kinetic parameters	
	k_{ap} (min^{-1})	R^2
Control	2.2×10^{-4}	0.94
TiO$_2$_EtOH	0.04	0.90
TiO$_2$_IPA	0.03	0.97
TiO$_2$_H$_2$O	0.02	0.99

[a] Reaction conditions: [TC] in the dark = 12, 24, 19 mg L^{-1} for the solutions with TiO$_2$_EtOH, TiO$_2$_IPA and TiO$_2$_H$_2$O nanopowders. V_{TC} = 50 mL, m_{catal} = 25 mg, reaction time = 30 min, source of light: simulated solar light.

the pseudo-first-order kinetic model's eqn (S12).† The kinetic parameters can be found in Table 3.

Comparing the rate constant (k_{ap}) values in Table 3 with previous studies, Safari et al.[141] reported similar rate constant values when using nanosized TiO$_2$ for the photodegradation of TC in aqueous solutions under UV light (k_{ap} = 2.49 × 10^{-2} min^{-1}, [TC]$_{initial}$ = 27 mg L^{-1}). Bouafia-Chergui et al.[142] also reported the photocatalytic degradation of TC in water using TiO$_2$ as a photocatalyst also under UV light. The most concentrated solution had an initial tetracycline's concentration of 20 mg L^{-1} and the obtained apparent rate constant value was 2.1 × 10^{-2} min^{-1}. Again, this value is in line with the present results for TiO$_2$ nanopowders; however, in this study solar radiation was used, which adds significant environmental value, with the incorporation of renewable sunlight energy and not being restricted just to UV radiation. Moreover, it is worth mentioning that this work reports a simple and fast microwave synthesis (10 min at 200 °C) of TiO$_2$ nanostructures by employing non-toxic reagents, which showed excellent ability for the removal of tetracycline molecules from polluted water.

Recyclability tests. To determine the stability of the photocatalysts, reusability tests were performed in the presence of the best photocatalyst (the TiO$_2$_EtOH nanopowder) under a simulated solar light source. For the second cycle, as seen in Fig. 13(a), little adsorption (~15%) occurred within 240 min (4 h) in the dark (no regeneration). This result may be due to the fact that tetracycline molecules are blocking all active sites around the photocatalyst. After the completion of the second cycle, the TiO$_2$ nanopowder without regeneration was observed through SEM (Fig. 13(b)). A clear thick layer is wrapping the photocatalyst structures, which is thought to be causing the significant loss of TC adsorption's capability. It also impacted the overall percentage of TC removal, and the material can only reach 40% of TC degradation, compared to the initial 88% (Fig. 12(a)). To fully recover the adsorption capacity of the photocatalyst, a strategy based on UV exposure was explored, since it is simple to implement in a real production process.[72] After the first cycle (adsorption + photocatalytic activity), the TiO$_2$_EtOH nanopowder was exposed for 4 h to UV light irradiation in an aqueous solution. A complete recovery is observed in terms of TC adsorption (~60% after 240 min in the dark) and overall TC removal (~80% is obtained after 240 min in the dark + 30 min of light exposure), see Fig. 12(a). In contrast with the TiO$_2$ nanopowder without regeneration, the SEM image of the nanopowder treated with UV light shows the presence of well-defined particles without a coating layer (Fig. 13(b)), which confirms the total recovery. To the best of our knowledge, there are no other studies in the literature showing similar SEM images of nanostructures encapsulated/coated with tetracycline compounds and/or products from the photodegradation reaction of tetracycline.

Reactive oxygen species (ROS) experiments. The influence of different reactive oxygen species (ROS) on the degradation rate of TC using the TiO$_2$_EtOH nanopowder was investigated under simulated solar light and after 240 min in the dark (Fig. S9†). Several ROS contribute to the photocatalytic degradation process, encompassing holes (h$^+$), hydroxyl ($^\bullet$OH), superoxide ions ($^\bullet$O$_2^-$), singlet oxygen (^{1}O$_2$) radicals and electrons (e$^-$).[74,143,144] As shown in Fig. S9,† a reduction in the degradation percentages can be observed upon the use of p-benzoquinone
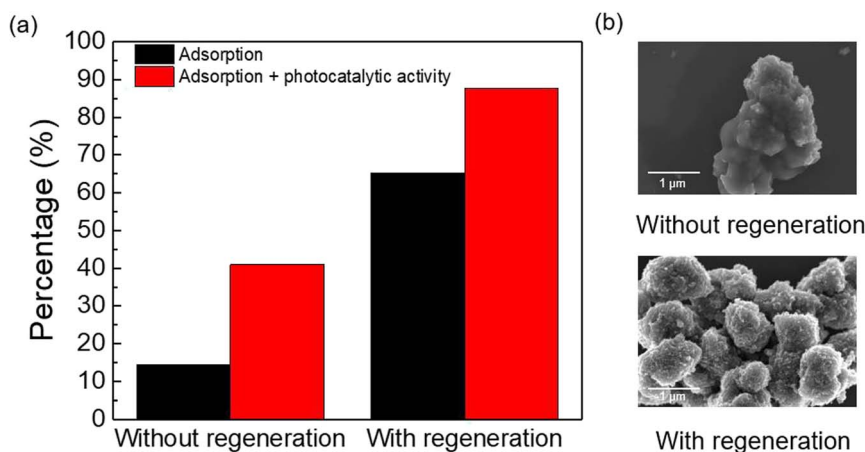
Fig. 13 (a) Comparison of TC adsorption (240 min in the dark) and adsorption followed by photocatalytic activity (240 min in the dark + 30 min of simulated solar light exposure) without and with a UV exposure regeneration of 240 min (both corresponding to the second cycle of reutilization). (b) SEM images of the TiO$_2$_EtOH nanopowder without and with regeneration.

**728** | Environ. Sci.: Adv., 2025, **4**, 713–738

© 2025 The Author(s). Published by the Royal Society of Chemistry

(BQ) and sodium azide (SA) scavengers. This indicates that $^{\cdot}O_2^-$ and $^1O_2$ radicals are the main active species involved in the degradation process of TC. These findings are well aligned with earlier research reporting the presence of superoxide radical species in the degradation process of tetracycline over TiO_2 nanostructures.[17,106,145,146] Regarding the generation of singlet oxygen radical species, several pathways have been proposed in the literature.[147] Nevertheless, surface defects that can act as both reactive sites and trapping sites might enhance the photocatalytic performance. Studies indicated that the existence of surface oxygen vacancies (VOs) can be further reduced into superoxide anions and then converted into singlet oxygen.[148,149] Although the existence of surface oxygen vacancies could not be confirmed by XPS and photoluminescence spectroscopy analyses, the surface defects of the photocatalyst, as observed

through STEM, may be associated with the origin of these reactive species.

Structural characterization of the PU foams

The photocatalytic experiments with the TiO_2_EtOH nanopowder showed enhanced overall adsorption and degradation of tetracycline molecules compared with the other solvents (*i.e.*, nanopowders with isopropanol and water). Therefore, this nanopowder was chosen for further impregnation on PU foams to avoid costly recovery processes of nanopowders and guarantee the sustainable character of the materials produced. The photodegradation of tetracycline under simulated solar light and ecotoxicity assays against *Artemia salina* were both conducted in the presence of these functionalized TiO_2 PU Foams.
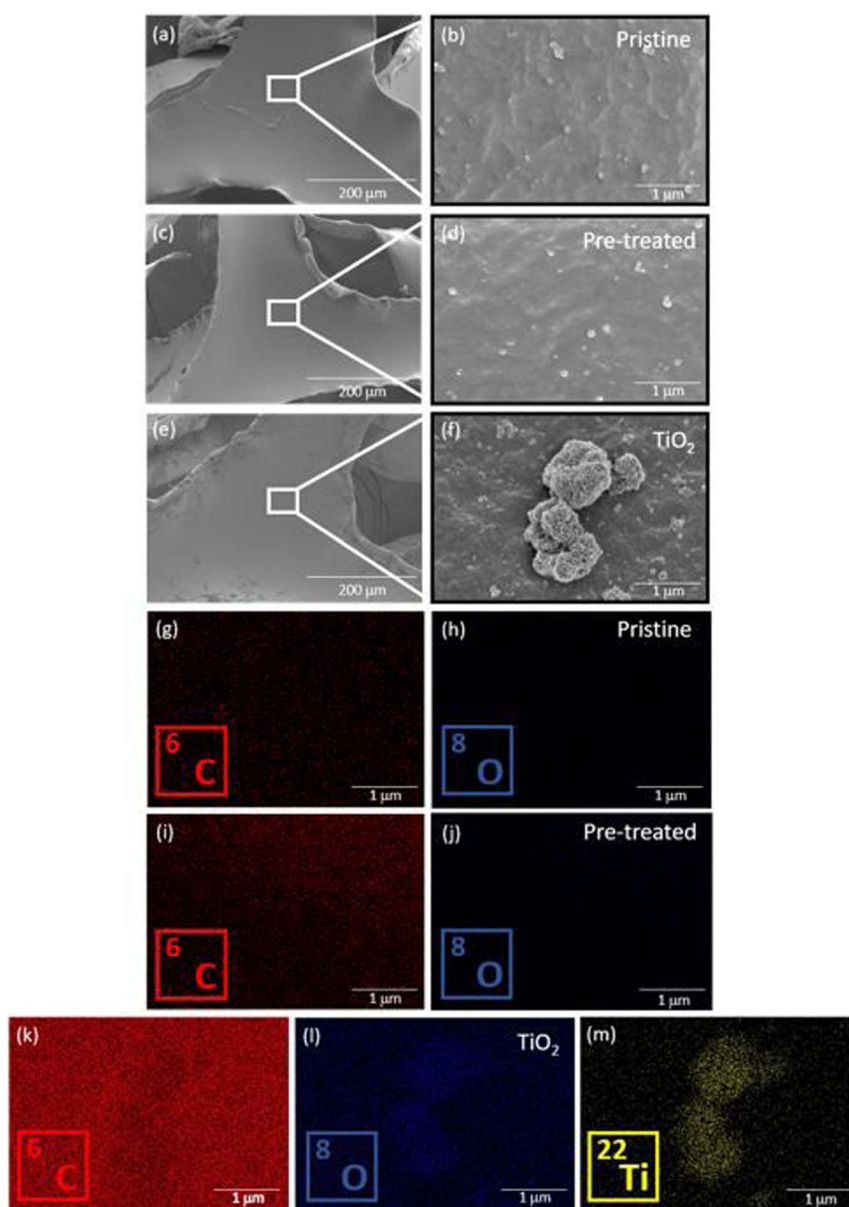
Fig. 14   SEM images of the PU foams. (a and b) Pristine PU foam; (c and d) pre-treated PU foam and (e and f) pre-treated PU foam after dip-coating of the TiO_2 nanomaterials synthesized with ethanol. The corresponding EDS maps of C (g, i and k); O (h, j and l); and Ti (m) are presented.

SEM/EDS. The PU foams observed by SEM showed a typical cellular structure specific to polyurethane foams (Fig. S10†).[150,151] The pores of the commercial PU foam were in the millimeter range (Fig. S10†). From the SEM images, it is possible to observe that the surface of the pristine PU foam is smooth without any macro-sized defects and crack-free, but with wrinkling edges (Fig. 14(a)). In the micrometer range, it was possible to observe artifacts throughout its surface (Fig. 14(b)). The PU foams were also observed after the NaOH treatment (pre-treated) and no clear difference could be inferred when compared to the pristine PU foam (Fig. 14(c and d)). Nevertheless, when the pre-treated PU foam after the dip-coating process was observed, the differences became evident (Fig. 14(e and f)), even at the macro-scale, with the presence of some agglomerates on the wrinkling edges of the PU foam resultant from the deposition process (Fig. 14(e)). SEM images (Fig. 14(a and b)) show that the TiO_2 nanomaterials synthesized with ethanol as solvent resulted in micrometer TiO_2 aggregates, and after the dip-coating process, these aggregates are still discernible. The artifacts observed in the pristine and pre-treated PU foams can still be observed after the deposition process, however, other smaller structures were observed, suggesting the presence of dispersed TiO_2 particles or smaller TiO_2 aggregates in the foam surface.

Pristine PU foam, pre-treated PU foam and pre-treated PU foam after dip-coating of the TiO_2_EtOH nanomaterial were also analysed using EDS. The analyses were carried out simultaneously in the same areas of the SEM images for all the PU foams. EDS analysis confirmed that the pre-treatment with NaOH did not leave residues at the surface of the substrates, since no impurities were detected, *i.e.*, sodium. Both pristine and pre-treated PU foams were composed of C and O, which is expected for polyurethane foam substrates[152] (Fig. 14(g–j)). In Fig. 14(k–m), not only C and O are observed from the substrate, but also Ti and O are present on the TiO_2 agglomerates. Ti was also detected throughout the foam surface as can be observed from the Ti EDS map in Fig. 14(m). Based on the EDS analyses, it can be inferred that the NaOH surface treatment assisted the immobilization of the TiO_2 nanostructures in the PU surface.

Photocatalytic degradation of tetracycline using the pre-treated PU foams. The photocatalytic activity of the pre-treated PU foams, with and without the photocatalyst, was determined considering the degradation percentages when exposed to simulated solar light. The study in the absence of light was performed for 1 h to achieve adsorption–desorption equilibrium. After this time, it can be seen that both pristine (uncoated) and pre-treated TiO_2 PU foam did not adsorb TC molecules (Fig. 15). Despite the microporosity, the foam's surface is flat and smooth (Fig. 14(c and d)), leading to the low adsorption of tetracycline molecules observed with the pristine PU foam during the dark phase. Regarding the pre-treated TiO_2 PU foam, as seen previously in Fig. 12(a), the TiO_2 nanopowder showed significantly high adsorption towards molecules of tetracycline during the dark phase. Throughout this process, the surface area played an important role. In contrast with the use of nanopowder, upon immobilization on a PU foam
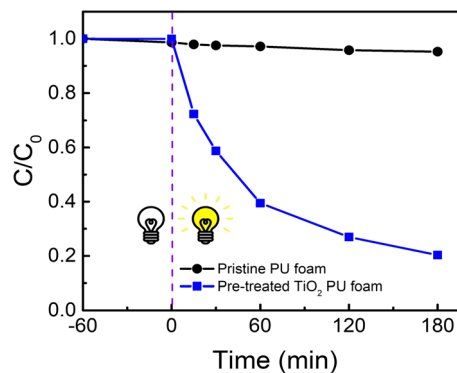

Fig. 15 Degradation profiles of tetracycline over PU foams (pristine and pre-treated TiO_2 PU foam) in the dark (for 60 min) and under simulated solar light (for 180 min). The black curve represents the C/C_0 over time for the pristine foam (uncoated), while the blue curve is for the pre-treated TiO_2 PU foam.

(Fig. 15), this adsorption was almost null. A possible explanation could be related to the use of polyacrylic acid in the dip-coating process, impacting the adsorption mechanism of the photocatalysts. This polymer may be blocking the available sites on the surface of the photocatalyst. Nevertheless, under light irradiation a notable decay in the concentration of tetracycline is observed in the presence of the TiO_2 PU foam, in comparison with the pristine PU foam, attesting the photocatalytic behavior of the TiO_2 nanostructures, Fig. 15, by reaching around 80% of TC degradation in 180 min of light exposure.

The organic water pollutant photodegradation in the presence of semiconductors is achieved when the photocatalyst is exposed to light with an energy superior to its band gap energy; the photons' energy is absorbed, leading to the excitation of electrons from the valence band to the conduction band, and thus creating electron–hole pairs. If the recombination of electrons and holes does not occur, electrons and holes can migrate to the surface of the photocatalyst and participate in redox reactions. Holes will oxidize water molecules and form superoxide radical species ($OH^•$). Simultaneously, electrons will reduce oxygen molecules and generate hydroxyl radicals ($O_2^{•−}$). The superoxide radicals will be afterwards protonated to harvest hydro-peroxyl radicals ($HOO^•$) and thereafter hydrogen peroxide (H_2O_2) and hydroxyl radicals are formed.[153–156] These hydroxyl radical species will be further responsible for the transformation of tetracycline molecules into different intermediates. Although multiple degradation pathways could be proposed due to these various intermediates that may be formed, the ROS produced would attack the double bonds, aromatic ring and amino group in tetracycline, typically *via* ring opening and cleavage of the central carbon bond reactions.[144,157,158] Smaller intermediates would be generated and eventually would be mineralized into some tiny molecules, such as CO_2, H_2O[159] and inorganic ions that are gradually formed *via* oxidation steps.[144]

Recyclability tests with the pre-treated TiO_2 PU foam. To verify the integrity of the TiO_2 PU foam, reusability tests were conducted under 5 consecutive cycles (Fig. 16). In each cycle, the
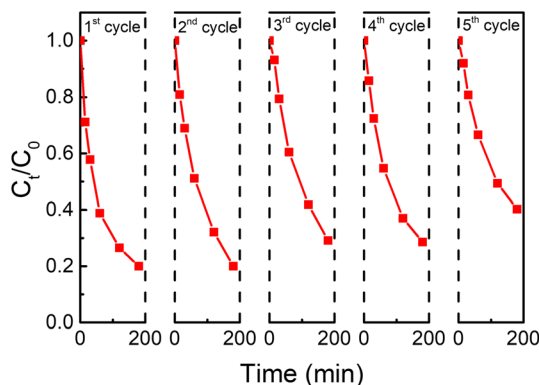
730 | *Environ. Sci.: Adv.*, 2025, **4**, 713–738

© 2025 The Author(s). Published by the Royal Society of Chemistry

Fig. 16 Photocatalytic recycling activity of pre-treated TiO$_2$ PU foam under 5 consecutive cycles, under simulated solar light for 180 min.

foam was exposed to solar light for 180 min. A minimal photocatalytic efficiency loss of around 20% was obtained upon completion of the fifth cycle. This indicates that the TiO$_2$ PU foam is stable[160] and can be reused up to 5 cycles. In fact, the dip-coating method enables a good adhesion of the nanomaterials to different substrates with various compositions and intricate geometrical structures, as previously demonstrated.[161] Moreover, studies have shown that the polymer used for dip-coating (PAA) is compatible with this technique.[162,163] The present results demonstrate that reusable photocatalysts with high degradation efficiency towards water pollutants can be produced in an effective and affordable manner while avoiding the issues associated with the recovery of powdered photocatalysts.

Ecotoxicity assays. Exposure studies on *Artemia salina* (nauplii) were conducted in the presence of the pre-treated TiO$_2$ PU foams to examine the effects of the functionalized substrates on the marine ecosystems. The mortality (%) was determined under acute exposure for 24 h with the PU foams, (without photocatalyst, with pre-treatment and photocatalyst), as well as with the negative control (artificial seawater) and positive control (10% DMSO), see eqn (1). The mortality rate (%) for *Artemia* is shown in Table 4. As expected, the pre-treated TiO$_2$ PU foam exhibits a slightly higher mortality percentage compared with the foam without the catalyst. This may be related to the photocatalytic behavior of TiO$_2$ under light irradiation and the generation of ROS causing oxidative stress on the organisms.[164] However, the aim of the utilization of

a polymer (in this case, polyacrylic acid) to coat the TiO$_2$ nanostructures is not only to promote a better adhesion of the nanostructures to the PU foam but also to minimize possible toxic effects on aquatic organisms. According to the literature, polyacrylic acid can hinder the formation of ROS by TiO$_2$ nanostructures and help mitigate their phototoxicity under sunlight.[165] Most importantly, it should be noted that the functionalized substrates presented very low mortality (<10%), and hence, are considered safe for aquatic species.[166] As for current eco-toxicological studies, these often assess the toxicity effects with suspensions of nanoparticles,[75,166–168] rather than determining the acute toxicity of nanoparticles functionalized on substrates to aquatic organisms, as herein investigated.

Conclusions

Solar-light-driven TiO$_2$ photocatalysts on 3D polyurethane foams were developed with the aid of microwave irradiation and a dip-coating method. Microwave synthesis of TiO$_2$ nanopowders was performed at 200 °C for 10 min in the presence of different solvents (ethanol, IPA and water). Pure anatase was obtained for the synthesis in ethanol, whereas in IPA and H$_2$O, a mixture of anatase/brookite or anatase/rutile phases was present, respectively, as revealed by XRD. SEM/STEM results revealed highly porous micro-sized spherical/elongated TiO$_2$ aggregates composed of fine nanocrystals for the TiO$_2$_EtOH nanomaterial. These TiO$_2$ nanocrystals had low and high-index facets, while the latter presented bulk/surface structural defects. For the syntheses using IPA and water, 1D nanostructures were formed together with other smaller nanocrystals with an undefined shape. A higher contribution from the defect states for the TiO$_2$ ethanol nanopowder was also suggested based on the photoluminescence measurements. BET analysis confirmed that the specific surface area of the porous TiO$_2$ synthesized with ethanol was superior to the nanopowders synthesized with IPA and H$_2$O, thus conferring it enhanced capacity for surface oxygen adsorption, as observed through XPS. This characteristic enabled a high TC sorption efficiency (~58% in 240 min). Reusability tests demonstrated that UV exposure effectively restored its adsorption capacity and overall performance for the removal of TC. Although TC adsorption was suppressed when TiO$_2$ nanostructures were incorporated into a PU foam, almost the same percentage of TC removal from aqueous systems could be obtained (~80% in 180 min of solar light exposure with the TiO$_2$ PU foam and ~88% with the TiO$_2$_EtOH nanopowder after 240 min in the dark + 30 min of solar light exposure). Moreover, the exposure of TiO$_2$ PU foams to aquatic organisms had no significant toxic effects after 24 h. In summary, this study highlighted the production of reusable 3D TiO$_2$ PU foams with a strong ability to remove water pollutants, such as antibiotics, by the combination of a fast microwave-assisted approach and a simple dip-coating technique.

Data availability

The data supporting this article have been included as part of the ESI.†

Table 4 Mortality rate (%) for *Artemia salina* (nauplii) measured for 24 h exposure to pristine (without photocatalyst) and pre-treated PU foam (with the TiO$_2$ photocatalyst). Mean ± SEM, $n = 5$

	Mortality (%)	Standard error of the mean (%)
Negative control (*Artemia* salt)	2	1.79
PU foam (without) photocatalyst	2	1.79
Pre-treated PU foam (with photocatalyst)	8	4.92
Positive control (10% DMSO)	100	0

Author contributions

All authors reviewed and approved the final version of the manuscript for publication.

Conflicts of interest

The authors declare no conflict of interest.

Acknowledgements

References

1 L. Lin, H. Yang and X. Xu, Effects of Water Pollution on Human Health and Disease Heterogeneity: A Review, *Front. Environ. Sci.*, 2022, **10**, 880246.

2 D. Ghime, P. Ghosh, D. Ghime and P. Ghosh, in *Advanced Oxidation Processes - Applications, Trends, and Prospects*, ed. C. Bustillo-Lecompte, IntechOpen, 2020.

3 A. Patel, A. Arkatkar, S. Singh, A. Rabbani, J. D. Solorza Medina, E. S. Ong, M. M. Habashy, D. A. Jadhav, E. R. Rene, A. A. Mungray and A. K. Mungray, Physicochemical and biological treatment strategies for converting municipal wastewater and its residue to resources, *Chemosphere*, 2021, **282**, 130881.

4 S. J. Kimosop, Z. M. Getenga, F. Orata, V. A. Okello and J. K. Cheruiyot, Residue levels and discharge loads of antibiotics in wastewater treatment plants (WWTPs), hospital lagoons, and rivers within Lake Victoria Basin, Kenya, *Environ. Monit. Assess.*, 2016, **188**(532), 1–9.

5 S. Zheng, Y. Wang, C. Chen, X. Zhou, Y. Liu, J. Yang, Q. Geng, G. Chen, Y. Ding and F. Yang, Current Progress in Natural Degradation and Enhanced Removal Techniques of Antibiotics in the Environment: A Review, *Int. J. Environ. Res. Publ. Health*, 2022, **19**(17), 1–31.

6 G. Gopal, S. A. Alex, N. Chandrasekaran and A. Mukherjee, A review on tetracycline removal from aqueous systems by advanced treatment techniques, *RSC Adv.*, 2020, **10**(45), 27081–27095.

7 A. Fiaz, D. Zhu and J. Sun, Environmental fate of tetracycline antibiotics: degradation pathway mechanisms, challenges, and perspectives, *Environ. Sci. Eur.*, 2021, **33**(64), 1–17.

8 H. Zhu, M. Li, L. Zou, Y. Hu, H. Hao, J. Dou and J. Mao, A study on singlet oxygen generation for tetracycline degradation *via* modulating the size of α-Fe$_2$O$_3$ nanoparticle anchored on g-C$_3$N$_4$ nanotube photocatalyst, *Nano Res.*, 2023, **16**(2), 2236–2244.

9 M. Bortolanza, B. L. Santos-Lobato, G. C. Nascimento and E. Del-Bel, in *Diagnosis and Management in Parkinson's Disease: the Neuroscience of Parkinson's Disease*, ed. C. R. Martin and V. R. Preedy, Academic Press, 2020, vol. 1, pp. 491–510.

10 S. Tariq, S. F. A. Rizvi and U. Anwar, Tetracycline: Classification, Structure Activity Relationship and Mechanism of Action as a Theranostic Agent for Infectious Lesions-A Mini Review, *Biomed J Sci Tech Res*, 2018, **7**, 1–10.

11 I. Janser, in *Bioactive Carboxylic Compound Classes: Pharmaceuticals and Agrochemicals*, ed. C. Lamberth and J. Dinges, John Wiley & Sons, Ltd, 2016, pp. 115–131.

12 A. Rusu and E. L. Buta, The development of third-generation tetracycline antibiotics and new perspectives, *Pharmaceutics*, 2021, **13**, 2085.

13 G. Gopal, S. A. Alex, N. Chandrasekaran and A. Mukherjee, A review on tetracycline removal from aqueous systems by advanced treatment techniques, *RSC Adv.*, 2020, **10**, 27081–27095.

14 J. Chico, F. van Holthoon and T. Zuidema, Ion Suppression Study for Tetracyclines in Feed, *Chromatogr. Res. Int.*, 2012, **2012**, 1–9.

15 A. di Cerbo, F. Pezzuto, G. Guidetti, S. Canello and L. Corsi, Tetracyclines: Insights and Updates of their Use in Human and Animal Pathology and their Potential Toxicity, *Open Biochem. J.*, 2019, **13**, 1–12.

16 C. Gu and K. G. Karthikeyan, Interaction of tetracycline with aluminum and iron hydrous oxides, *Environ. Sci. Technol.*, 2005, **39**(8), 2660–2667.

17 M. Sharma, M. K. Mandal, S. Pandey, R. Kumar and K. K. Dubey, Visible-Light-Driven Photocatalytic Degradation of Tetracycline Using Heterostructured Cu$_2$O-TiO$_2$ Nanotubes, Kinetics, and Toxicity Evaluation of Degraded Products on Cell Lines, *ACS Omega*, 2022, **7**(37), 33572–33586.

18 O. Baaloudj, I. Assadi, N. Nasrallah, A. El Jery, L. Khezami and A. A. Assadi, Simultaneous removal of antibiotics and inactivation of antibiotic-resistant bacteria by photocatalysis: A review, *J. Water Proc. Eng.*, 2021, **42**, 1–11.

19 K. O'Dowd, K. M. Nair and S. C. Pillai, Photocatalytic degradation of antibiotic-resistant genes and bacteria using 2D nanomaterials: What is known and what are the challenges?, *Curr. Opin. Green Sustainable Chem.*, 2021, **30**, 1–7.

20 M. Malakotian, S. N. Asadzadeh, M. Khatami, M. Ahmadian, M. R. Heidari, P. Karimi, N. Firouzeh and R. S. Varma, Protocol encompassing ultrasound/Fe_3O_4 nanoparticles/persulfate for the removal of tetracycline antibiotics from aqueous environments, *Clean Technol. Environ. Policy*, 2019, **21**, 1665–1674.

21 A. G. Capodaglio, Critical Perspective on Advanced Treatment Processes for Water and Wastewater: AOPs, ARPs, and AORPs, *Appl. Sci.*, 2020, **10**(13), 4549.

22 H. Liu, C. Wang and G. Wang, Photocatalytic Advanced Oxidation Processes for Water Treatment: Recent Advances and Perspective, *Chem. Asian J.*, 2020, **15**, 3239–3253.

23 I. A. Saleh, N. Zouari and M. A. Al-Ghouti, Removal of pesticides from water and wastewater: Chemical, physical and biological treatment approaches, *Environ. Technol. Innovation*, 2020, **19**(4), 101026.

24 E. M. Abd El-Monaem, M. Hosny and A. S. Eltaweil, Synergistic effect between adsorption and Fenton-like degradation on CoNiFe-LDH/ZIF-8 composite for efficient degradation of doxycycline, *Chem. Eng. Sci.*, 2024, **287**, 119707.

25 E. M. Abd El-Monaem, N. Al Harby, M. El Batouti and A. S. Eltaweil, Enhanced Redox Cycle of Rod-Shaped MIL-88A/$SnFe_2O_4$@MXene Sheets for Fenton-like Degradation of Congo Red: Optimization and Mechanism, *Nanomaterials*, 2024, **14**, 54.

26 J. Wang and R. Zhuan, Degradation of antibiotics by advanced oxidation processes: An overview, *Sci. Total Environ.*, 2020, **701**, 135023.

27 P. Zawadzki, Visible Light–Driven Advanced Oxidation Processes to Remove Emerging Contaminants from Water and Wastewater: a Review, *Water, Air, Soil Pollut.*, 2022, **233**(9), 1–38.

28 Y. Mikhak, M. M. A. Torabi and A. Fouladitajar, in *Sustainable Water and Wastewater Processing*, ed. C. M. Galanakis and E. Agrafioti, Elsevier, 2019, pp. 55–91.

29 E. M. Abd El-Monaem, H. M. Elshishini, S. S. Bakr, H. G. El-Aqapa, M. Hosny, G. Andaluri, G. M. El-Subruiti, A. M. Omer and A. S. Eltaweil, A comprehensive review on LDH-based catalysts to activate persulfates for the degradation of organic pollutants, *npj Clean Water*, 2023, **6**, 1–24.

30 J. M. Coronado and M. D. Hernández-Alonso, in Design of Advanced Photocatalytic Materials for Energy and Environmental Applications, *Green Energy and Technology*, Springer, London, 2013, vol. 71, pp. 85–101.

31 F. M. dela Rosa, M. Popović, J. Papac Zjačić, G. Radić, M. Kraljić Roković, M. Kovačić, M. J. Farré, B. Genorio, U. Lavrenčič Štangar, H. Kušić, A. Lončarić Božić and M. Petrović, Visible-Light Activation of Persulfate or H_2O_2 by Fe_2O_3/TiO_2 Immobilized on Glass Support for Photocatalytic Removal of Amoxicillin: Mechanism, Transformation Products, and Toxicity Assessment, *Nanomaterials*, 2022, **12**(23), 4328.

32 M. L. Matias, A. S. Reis-Machado, J. Rodrigues, T. Calmeiro, J. Deuermeier, A. Pimentel, E. Fortunato, R. Martins and D. Nunes, Microwave Synthesis of Visible-Light-Activated g-C_3N_4/TiO_2 Photocatalysts, *Nanomaterials*, 2023, **13**(6), 1090.

33 G. P. Barreto, G. Morales and M. L. L. Quintanilla, Microwave Assisted Synthesis of ZnO Nanoparticles: Effect of Precursor Reagents, Temperature, Irradiation Time, and Additives on Nano-ZnO Morphology Development, *J. Mater.*, 2013, **2013**, 1–11.

34 D. E. González-Anota, S. P. Paredes-Carrera, R. M. Pérez-Gutierrez, B. Arciniega-Caballero, R. Borja-Urby, J. C. Sánchez-Ochoa and E. Rojas-García, Green Synthesis by Microwave Irradiation of TiO_2 Using Cinnamomum verum and the Application in Photocatalysis, *J. Chem.*, 2023, **2023**, 1–17.

35 R. N. Gedye, F. E. Smith, A. N. D Kenneth Charles Westaway and K. Charles Westaway, The rapid synthesis of organic compounds in microwave ovens, *Can. J. Chem.*, 1988, **66**, 17–26.

36 A. Pimentel, J. Rodrigues, P. Duarte, D. Nunes, F. M. Costa, T. Monteiro, R. Martins and E. Fortunato, Effect of solvents on ZnO nanostructures synthesized by solvothermal method assisted by microwave radiation: a photocatalytic study, *J. Mater. Sci.*, 2015, **50**(17), 5777–5787.

37 A. Pimentel, D. Nunes, S. Pereira, R. Martins and E. Fortunato, in *Semiconductor Photocatalysis – Materials, Mechanisms and Applications*, IntechOpen, 2016, ch. 3.

38 R. S. Jalawkhan, A. A. Ouda, A. M. Abdul-Lettif and F. K. Mohamad Alosfur, Effect of solvents on the morphology of TiO_2 nanoparticles prepared by microwave method, *IOP Conf. Ser. Mater. Sci. Eng.*, 2020, **928**(7), 072159.

39 R. Krishnapriya, S. Praneetha and A. Vadivel Murugan, Microwave-solvothermal synthesis of different TiO_2 nano-morphologies with enhanced efficiency by incorporating Ni nanoparticles in an electrolyte for dye-sensitized solar cells, *Inorg. Chem. Front.*, 2017, **4**, 1665–1678.

40 Y. C. Wu and Y. C. Tai, Effects of alcohol solvents on anatase TiO_2 nanocrystals prepared by microwave-assisted solvothermal method, *J. Nanopart. Res.*, 2013, **15**, 1–11.

41 M. Kardeş, H. C. Yatmaz and K. Öztürk, ZnO Nanorods Grown on Flexible Polyurethane Foam Surfaces for Photocatalytic Azo Dye Treatment, *ACS Appl. Nano Mater.*, 2023, **6**(8), 6605–6613.

42 R. Wang, D. Ren, S. Xia, Y. Zhang and J. Zhao, Photocatalytic degradation of Bisphenol A (BPA) using immobilized TiO_2 and UV illumination in a horizontal circulating bed photocatalytic reactor (HCBPR), *J. Hazard. Mater.*, 2009, **169**, 926–932.

43 M. Rico-santacruz, P. García-muñoz, V. Keller, N. Batail, C. Pham, D. Robert and N. Keller, Alveolar TiO_2-β-SiC photocatalytic composite foams with tunable properties for water treatment, *Catal. Today*, 2019, **328**, 235–242.

© 2025 The Author(s). Published by the Royal Society of Chemistry

Environ. Sci.: Adv., 2025, **4**, 713–738 | **733**

44 L. Ni, Y. Li, C. Zhang, L. Li, W. Zhang and D. Wang, Novel floating photocatalysts based on polyurethane composite foams modified with silver/titanium dioxide/graphene ternary nanoparticles for the visible-light-mediated remediation of diesel-polluted surface water, *J. Appl. Polym. Sci.*, 2016, **133**(19), 1–9.

45 V. Porley and N. Robertson, in *Nanostructured Photocatalysts: from Materials to Applications in Solar Fuels and Environmental Remediation*, Elsevier, 2020, pp. 129–171.

46 A. M. Nasir, J. Jaafar, F. Aziz, N. Yusof, W. N. W. Salleh, A. F. Ismail and M. Aziz, A review on floating nanocomposite photocatalyst: Fabrication and applications for wastewater treatment, *J. Water Proc. Eng.*, 2020, **36**, 101300.

47 M. Alam, N. M. Alandis, F. Zafar, E. Sharmin and Y. M. Al-Mohammadi, Polyurethane-TiO$_2$ nanocomposite coatings from sunflower- oil-based amide diol as soft segment, *J. Macromol. Sci., Part A: Pure Appl. Chem.*, 2018, **55**, 698–708.

48 L. Polo Fonseca, A. Duval, E. Luna, M. Ximenis, S. De Meester, L. Avérous and H. Sardon, Reducing the carbon footprint of polyurethanes by chemical and biological depolymerization: Fact or fiction?, *Curr. Opin. Green Sustainable Chem.*, 2023, **41**, 100802.

49 E. Mendiburu-Valor, T. Calvo-Correas, L. Martin, I. Harismendy, C. Peña-Rodriguez and A. Eceiza, Synthesis and characterization of sustainable polyurethanes from renewable and recycled feedstocks, *J. Clean. Prod.*, 2023, **400**, 136749.

50 L. Gausas, S. K. Kristensen, H. Sun, A. Ahrens, B. S. Donslund, A. T. Lindhardt and T. Skrydstrup, Catalytic Hydrogenation of Polyurethanes to Base Chemicals: From Model Systems to Commercial and End-of-Life Polyurethane Materials, *JACS Au*, 2021, **1**(4), 517–524.

51 B. Li, X. Liu, X. Zhang, J. Zou, W. Chai and Y. Lou, Rapid adsorption for oil using superhydrophobic and superoleophilic polyurethane sponge, *J. Chem. Technol. Biotechnol.*, 2015, **90**(11), 2106–2112.

52 M. El Bouraie and A. Abdelghany, Sorption Features of Polyurethane Foam Functionalized with Salicylate for Chlorpyrifos: Equilibrium, Kinetic Models and Thermodynamic Studies, *Polymers*, 2020, **12**(9), 2036.

53 M. Valodkar, P. S. Rathore, P. Sharma, D. Kanchan, M. Patel and S. Thakore, Immobilization of metal nanoparticles on polyurethane membranes: Synthesis and electrical properties, *Polym. Int.*, 2012, **61**(12), 1745–1750.

54 T. Liu, S. Sun, L. Zhou, P. Li, Z. Su and G. Wei, Polyurethane-Supported Graphene Oxide Foam Functionalized with Carbon Dots and TiO$_2$ Particles for Photocatalytic Degradation of Dyes, *Appl. Sci.*, 2019, **9**, 293.

55 B. Domènech, K. Ziegler, N. Vigués, W. Olszewski, C. Marini, J. Mas, M. Muñoz, D. N. Muraviev and J. Macanás, Polyurethane foams doped with stable silver nanoparticles as bactericidal and catalytic materials for the effective treatment of water, *New J. Chem.*, 2016, **40**, 3716–3725.

56 J. Silica, M. Vittoria Diamanti, C. Antonini, M. Ferrari, D. Cho and J. Kyun Oh, Silica Nanoparticle-Infused

Omniphobic Polyurethane Foam with Bacterial Anti-Adhesion and Antifouling Properties for Hygiene Purposes, *Nanomaterials*, 2023, **13**(14), 2035.

57 F. Wu, J. Zheng, X. Ou and M. Liu, Two in One: Modified Polyurethane Foams by Dip-Coating of Halloysite Nanotubes with Acceptable Flame Retardancy and Absorbency, *Macromol. Mater. Eng.*, 2019, **304**, 1900213.

58 F. Wu, K. Pickett, A. Panchal, M. Liu and Y. Lvov, Superhydrophobic Polyurethane Foam Coated with Polysiloxane-Modified Clay Nanotubes for Efficient and Recyclable Oil Absorption, *ACS Appl. Mater. Interfaces*, 2019, **11**(28), 25445–25456.

59 A. Khandan Barani, G. Roudini, F. Barahuie and S. U. Binti Masuri, Design of hydrophobic polyurethane–magnetite iron oxide-titanium dioxide nanocomposites for oil-water separation, *Heliyon*, 2023, **9**(5), e15580.

60 M. Q. Seah, Z. C. Ng, W. J. Lau, M. Gürsoy, M. Karaman, T. W. Wong and A. F. Ismail, Development of surface modified PU foam with improved oil absorption and reusability *via* an environmentally friendly and rapid pathway, *J. Environ. Chem. Eng.*, 2022, **10**(1), 106817.

61 D. S. Pattanayak, J. Mishra, J. Nanda, P. K. Sahoo, R. Kumar and N. K. Sahoo, Photocatalytic degradation of cyanide using polyurethane foam immobilized Fe-TCPP-S-TiO$_2$-rGO nano-composite, *J. Environ. Manage.*, 2021, **297**, 113312.

62 K. P. O. Mahesh, D.-H. Kuo, B.-R. Huang, M. Ujihara and T. Imae, Chemically modified polyurethane-SiO$_2$/TiO$_2$ hybrid composite film and its reusability for photocatalytic degradation of Acid Black 1 (AB 1) under UV light, *Appl. Catal., A*, 2014, **475**, 235–241.

63 T. Swift, L. Swanson, M. Geoghegan and S. Rimmer, The pH-responsive behaviour of poly(acrylic acid) in aqueous solution is dependent on molar mass, *Soft Matter*, 2016, **12**, 2542–2549.

64 S. A. Free, J. C. Bertolini, C. Y. Chan and M. J. Albero, *US Pat.*, US20070191502A1, 2007.

65 K. Pinato, K. Suttiponparnit, S. Jinawath and D. P. Kashima, TiO$_2$-coated alveolar clay foam as a photocatalyst for water detoxification, *J. Mater. Sci.*, 2020, **55**(11), 1451–1463.

66 C. A. Schneider, W. S. Rasband and K. W. Eliceiri, NIH Image to ImageJ: 25 years of image analysis, *Nat. Methods*, 2012, **9**(7), 671–675.

67 ISO 9277, *Determination of the Specific Surface Area of Solids by Gas Adsorption—BET Method*, ISO–International Standardization Organization, Geneva, Switzerland, 2nd edn, 2010.

68 D. Nunes, A. Pimentel, L. Santos, P. Barquinha, E. Fortunato and R. Martins, Photocatalytic TiO$_2$ Nanorod Spheres and Arrays Compatible with Flexible Applications, *Catalysts*, 2017, **7**(2), 60.

69 S. Singla, P. Devi and S. Basu, Highly Effectual Photocatalytic Remediation of Tetracycline under the Broad Spectrum of Sunlight by Novel BiVO$_4$/Sb$_2$S$_3$ Nanocomposite, *Catalysts*, 2023, **13**(4), 731.

70 O. A. Ajala, S. O. Akinnawo, A. Bamisaye, D. T. Adedipe, M. O. Adesina, O. A. Okon-Akan, T. A. Adebusuyi, A. T. Ojedokun, K. A. Adegoke and O. S. Bello, Adsorptive

removal of antibiotic pollutants from wastewater using biomass/biochar-based adsorbents, *RSC Adv.*, 2023, **13**(7), 4678.

71 R. Matos, I. Kuźniarska-Biernacka, M. Rocha, J. H. Belo, J. P. Araújo, A. C. Estrada, J. L. Lopes, T. Shah, B. A. Korgel, C. Pereira, T. Trindade and C. Freire, Design and photo-Fenton performance of Graphene/CuS/Fe$_3$O$_4$ tertiary nanocomposites for Rhodamine B degradation, *Catal. Today*, 2023, **418**, 114132.

72 F. Dalto, I. Kuźniarska-Biernacka, C. Pereira, E. Mesquita, O. S. G. P. Soares, M. F. R. Pereira, M. J. Rosa, A. S. Mestre, A. P. Carvalho and C. Freire, Solar light-induced methylene blue removal over TiO$_2$/AC composites and photocatalytic regeneration, *Nanomaterials*, 2021, **11**(11), 1–24.

73 A. Rovisco, M. Morais, R. Branquinho, E. Fortunato, R. Martins and P. Barquinha, Microwave-Assisted Synthesis of Zn2SnO4 Nanostructures for Photodegradation of Rhodamine B under UV and Sunlight, *Nanomaterials*, 2022, **12**(12), 2119.

74 A. Rovisco, M. Morais, R. Branquinho, E. Fortunato, R. Martins and P. Barquinha, Microwave-Assisted Synthesis of Zn$_2$SnO$_4$ Nanostructures for Photodegradation of Rhodamine B under UV and Sunlight, *Nanomaterials*, 2022, **12**(12), 2119.

75 Y. Ozkan, I. Altinok, H. Ilhan and M. Sokmen, Determination of TiO$_2$ and AgTiO$_2$ Nanoparticles in Artemia salina: Toxicity, Morphological Changes, Uptake and Depuration, *Bull. Environ. Contam. Toxicol.*, 2016, **96**(1), 36–42.

76 M. Ates, J. Daniels, Z. Arslan and I. O. Farah, Effects of aqueous suspensions of titanium dioxide nanoparticles on Artemia salina: assessment of nanoparticle aggregation, accumulation, and toxicity, *Environ. Monit. Assess.*, 2013, **185**(4), 3339–3348.

77 J. Lu, S. Tian, X. Lv, Z. Chen, B. Chen, X. Zhu and Z. Cai, TiO$_2$ nanoparticles in the marine environment: Impact on the toxicity of phenanthrene and Cd^{2+}o marine zooplankton Artemia Salina, *Sci. Total Environ.*, 2018, **615**, 375–380.

78 T. Ferreira-Gonçalves, A. Iglesias-Mejuto, T. Linhares, J. M. P. Coelho, P. Vieira, P. Faísca, J. Catarino, P. Pinto, D. Ferreira, H. A. Ferreira, M. M. Gaspar, L. Durães, C. A. García-González and C. P. Reis, Biological Thermal Performance of Organic and Inorganic Aerogels as Patches for Photothermal Therapy, *Gels*, 2022, **8**(8), 485.

79 J. Lopes, T. Ferreira-Gonçalves, L. Ascensão, A. S. Viana, L. Carvalho, J. Catarino, P. Faísca, A. Oliva, D. P. C. de Barros, C. M. P. Rodrigues, M. M. Gaspar and C. P. Reis, Safety of Gold Nanoparticles: From *In Vitro* to *In Vivo* Testing Array Checklist, *Pharmaceutics*, 2023, **15**(4), 1120.

80 Y. Morishima, M. Kobayashi, V. Petrykin, M. Kakihana and K. Tomita, Microwave-assisted hydrothermal synthesis of brookite nanoparticles from a water-soluble titanium complex and their photocatalytic activity, *J. Ceram. Soc. Jpn.*, 2007, **115**, 826–830.

81 A. Di Paola, M. Bellardita and L. Palmisano, Brookite, the Least Known TiO$_2$ Photocatalyst, *Catalysts*, 2013, **3**, 36–73.

82 L. P. Delgado, M. Z. Figueroa-Torres, M. C. Ceballos-Chuc, R. García-Rodríguez, J. J. Alvarado-Gil, G. Oskam and G. Rodriguez-Gattorno, Tailoring the TiO$_2$ phases through microwave-assisted hydrothermal synthesis: Comparative assessment of bactericidal activity, *Mater. Sci. Eng. C*, 2020, **117**, 111290.

83 C. Bandas, C. Lazau, A. Dabici, P. Sfirloaga, N. Vaszilcsin, I. Grozescu and V. Tiponut, Microwave-Assisted Hydrothermal Method for Synthesis of Nanocrystalline Anatase TiO$_2$, *Chem. Bull. "Politeh." Univ. Timisoara*, 2011, **56**(70), 81–84.

84 F. Xu, Review of analytical studies on TiO$_2$ nanoparticles and particle aggregation, coagulation, flocculation, sedimentation, stabilization, *Chemosphere*, 2018, **212**, 662–677.

85 D. Nunes, A. Pimentel, J. V. Pinto, T. R. Calmeiro, S. Nandy, P. Barquinha, L. Pereira, P. A. Carvalho, E. Fortunato and R. Martins, Photocatalytic behavior of TiO$_2$ films synthesized by microwave irradiation, *Catal. Today*, 2016, **278**, 262–270.

86 D. R. G. Mitchell and G. Casillas, Secondary Electron Imaging in an Aberration-Corrected STEM, *Microsc. Today*, 2016, **24**, 22–27.

87 L. DeRita, J. Resasco, S. Dai, A. Boubnov, H. V. Thang, A. S. Hoffman, I. Ro, G. W. Graham, S. R. Bare, G. Pacchioni, X. Pan and P. Christopher, Structural evolution of atomically dispersed Pt catalysts dictates reactivity, *Nat. Mater.*, 2019, **18**(7), 746–751.

88 Z. Zhou, Y. Yu, Z. Ding, M. Zuo and C. Jing, Modulating High-Index Facets on Anatase TiO$_2$, *Eur. J. Inorg. Chem.*, 2018, **2018**, 683–693.

89 J. J. Carey and K. P. McKenna, Does Polaronic Self-Trapping Occur at Anatase TiO$_2$ Surfaces?, *J. Phys. Chem. C*, 2018, **122**, 27540–27553.

90 W. Yuan, J. Meng, B. Zhu, Y. Gao, Z. Zhang, C. Sun and Y. Wang, Unveiling the Atomic Structures of the Minority Surfaces of TiO$_2$ Nanocrystals, *Chem. Mater.*, 2018, **30**, 288–295.

91 H. G. Yang, C. H. Sun, S. Z. Qiao, J. Zou, G. Liu, S. C. Smith, H. M. Cheng and G. Q. Lu, Anatase TiO$_2$ single crystals with a large percentage of reactive facets, *Nature*, 2008, **453**(7195), 638–641.

92 Z. Liu, Y. Zheng, T. Gao, J. Zhang, X. Sun and G. Zhou, Fabrication of anatase TiO$_2$ tapered tetragonal nanorods with designed {100}, {001} and {101} facets for enhanced photocatalytic H2 evolution, *Int. J. Hydrogen Energy*, 2017, **42**(34), 21775–21785.

93 N. Roy, Y. Sohn and D. Pradhan, Synergy of low-energy {101} and high-energy {001} TiO$_2$ crystal facets for enhanced photocatalysis, *ACS Nano*, 2013, **7**(3), 2532–2540.

94 X. Han, B. Zheng, J. Ouyang, X. Wang, Q. Kuang, Y. Jiang, Z. Xie and L. Zheng, Control of anatase TiO$_2$ nanocrystals with a series of high-energy crystal facets *via* a fuorine-free strategy, *Chem.–Asian J.*, 2012, **7**(11), 2538–2542.

© 2025 The Author(s). Published by the Royal Society of Chemistry

Environ. Sci.: Adv., 2025, **4**, 713–738 | 735

95 J. Lin, Y. U. Heo, A. Nattestad, Z. Sun, L. Wang, J. H. Kim and S. X. Dou, 3D Hierarchical Rutile TiO_2 and Metal-free Organic Sensitizer Producing Dye-sensitized Solar Cells 8.6% Conversion Efficiency, *Sci. Rep.*, 2014, **4**, 1–8.

96 Z. Lai, F. Peng, H. Wang, H. Yu, S. Zhang and H. Zhao, A new insight into regulating high energy facets of rutile TiO_2, *J. Mater. Chem. A*, 2013, **1**(13), 4182–4185.

97 A. Holm, M. Hamandi, F. Simonet, B. Jouguet, F. Dappozze and C. Guillard, Impact of rutile and anatase phase on the photocatalytic decomposition of lactic acid, *Appl. Catal. B Environ.*, 2019, **253**, 96–104.

98 J. He, Y. en Du, Y. Bai, J. An, X. Cai, Y. Chen, P. Wang, X. Yang and Q. Feng, Facile Formation of Anatase/Rutile TiO_2 Nanocomposites with Enhanced Photocatalytic Activity, *Molecules*, 2019, **24**(16), 2996.

99 R. Ma and T. Chen, Checking the Synergetic Effect between Anatase and Rutile, *J. Phys. Chem. C*, 2019, **123**(32), 19479–19485.

100 X. Wei, G. Zhu, J. Fang and J. Chen, Synthesis, characterization, and photocatalysis of well-dispersible phase-pure anatase TiO_2 nanoparticles, *Int. J. Photoenergy*, 2013, **2013**(7268), 1–6.

101 M. Andrade-Guel, L. Diáz-Jiménez, D. Cortés-Hernández, C. Cabello-Alvarado, C. Ávila-Orta, P. Bartolo-Pérez and P. Gamero-Melo, Microwave assisted sol–gel synthesis of titanium dioxide using hydrochloric and acetic acid as catalysts, *Bol. Soc. Espanola Ceram. Vidr.*, 2019, **58**(4), 171–177.

102 E. Zhang, Y. Pan, T. Lu, Y. Zhu and W. Dai, Novel synthesis of S-doped anatase TiO_2 *via* hydrothermal reaction of Cu–Ti amorphous alloy, *Appl. Phys. Mater. Sci. Process*, 2020, **126**, 1–8.

103 L. Zhu, Q. Lu, L. Lv, Y. Wang, Y. Hu, Z. Deng, Z. Lou, Y. Hou and F. Teng, Ligand-free rutile and anatase TiO_2 nanocrystals as electron extraction layers for high performance inverted polymer solar cells, *RSC Adv.*, 2017, **7**, 20084–20092.

104 M. L. Matias, A. Pimentel, A. S. Reis-Machado, J. Rodrigues, J. Deuermeier, E. Fortunato, R. Martins and D. Nunes, Enhanced Fe-TiO_2 Solar Photocatalysts on Porous Platforms for Water Purification, *Nanomaterials*, 2022, **12**, 1005.

105 A. Hiji, T. Hanawa, T. Yokoi, P. Chen, M. Ashida and M. Kawashita, Time Transient of Calcium and Phosphate Ion Adsorption by Rutile Crystal Facets in Hanks' Solution Characterized by XPS, *Langmuir*, 2021, **37**, 3597–3604.

106 F. Wang, L. Sun, Y. Li, W. Zhan, X. Wang and X. Han, Hollow Anatase TiO_2 Octahedrons with Exposed High-Index {102} Facets for Improved Dye-Sensitized Photoredox Catalysis Activity, *Inorg. Chem.*, 2018, **57**(8), 4550–4555.

107 A. Ghobadi, T. G. Ulusoy, R. Garifullin, M. O. Guler and A. K. Okyay, A Heterojunction Design of Single Layer Hole Tunneling ZnO Passivation Wrapping around TiO_2 Nanowires for Superior Photocatalytic Performance, *Sci. Rep.*, 2016, **6**(30587), 1–15.

108 W. F. Zhang, M. S. Zhang and Z. Yin, Microstructures and visible photoluminescence of TiO_2 nanocrystals, *Phys. Status Solidi A*, 2000, **179**(2), 319–327.

109 C. Mercado, Z. Seeley, A. Bandyopadhyay, S. Bose and J. L. McHale, Photoluminescence of dense nanocrystalline titanium dioxide thin films: Effect of doping and thickness and relation to gas sensing, *ACS Appl. Mater. Interfaces*, 2011, **3**(7), 2281–2288.

110 M. P. F. Graça, C. Nico, M. Peres, M. A. Valente and T. Monteiro, Study of the optical and dielectric properties of TiO_2 nanocrystals prepared by the Pechini method, *J. Nanosci. Nanotechnol.*, 2012, **12**(11), 8600–8606.

111 D. K. Pallotti, L. Passoni, P. Maddalena, F. Di Fonzo and S. Lettieri, Photoluminescence Mechanisms in Anatase and Rutile TiO_2, *J. Phys. Chem. C*, 2017, **121**(16), 9011–9021.

112 K. Iijima, M. Goto, S. Enomoto, H. Kunugita, K. Ema, M. Tsukamoto, N. Ichikawa and H. Sakama, Influence of oxygen vacancies on optical properties of anatase TiO_2 thin films, *J. Lumin.*, 2008, **128**, 911–913.

113 H. Tang, H. Berger, P. E. Schmid, F. Lévy and G. Burri, Photoluminescence in TiO_2 anatase single crystals, *Solid State Commun.*, 1993, **87**(9), 847–850.

114 D. O. Scanlon, C. W. Dunnill, J. Buckeridge, S. A. Shevlin, A. J. Logsdail, S. M. Woodley, C. R. A. Catlow, M. J. Powell, R. G. Palgrave, I. P. Parkin, G. W. Watson, T. W. Keal, P. Sherwood, A. Walsh and A. A. Sokol, Band alignment of rutile and anatase TiO_2, *Nat. Mater.*, 2013, **12**, 798–801.

115 R. M. Garcia, R. Carleer, M. A. Pérez, J. P. Torres, Y. Gu, P. Samyn and J. Yperman, Fe-TiO_2/AC and Co-TiO_2/AC composites: Novel photocatalysts prepared from waste streams for the efficient removal and photocatalytic degradation of cibacron yellow F-4G dye, *Catalysts*, 2021, **11**(10), 1–24.

116 I. A. W. Tan, A. L. Ahmad and B. H. Hameed, Adsorption isotherms, kinetics, thermodynamics and desorption studies of 2,4,6-trichlorophenol on oil palm empty fruit bunch-based activated carbon, *J. Hazard. Mater.*, 2009, **164**(2–3), 473–482.

117 F. Yu, J. Ma and S. Han, Adsorption of tetracycline from aqueous solutions onto multi-walled carbon nanotubes with different oxygen contents, *Sci. Rep.*, 2014, **4**(5326), 1–8.

118 B. Ghanim, J. J. Leahy, T. F. O'Dwyer, W. Kwapinski, J. T. Pembroke and J. G. Murnane, Removal of hexavalent chromium (Cr(VI)) from aqueous solution using acid-modified poultry litter-derived hydrochar: adsorption, regeneration and reuse, *J. Chem. Technol. Biotechnol.*, 2022, **97**, 55–66.

119 L. Zhang, T. Ai, X. Tian and S. Dai, An efficient removal mechanism for different hydrophilic antibiotics from aquatic environments by Cu–Al–Fe–Cr quasicrystals, *RSC Adv.*, 2022, **12**, 9995.

120 D. N. R. de Sousa, S. Insa, A. A. Mozeto, M. Petrovic, T. F. Chaves and P. S. Fadini, Equilibrium and kinetic studies of the adsorption of antibiotics from aqueous solutions onto powdered zeolites, *Chemosphere*, 2018, **205**, 137–146.

121 G. W. Kajjumba, S. Emik, A. Öngen, H. K. Ö. Aydın, A. Serdar, G. W. Kajjumba, S. Emik, A. Öngen, H. K. Ö. Aydın and A. Serdar, in *Advanced Sorption Process Applications*, IntechOpen, 2018.

122 S. Álvarez-Torrellas, R. S. Ribeiro, H. T. Gomes, G. Ovejero and J. García, Removal of antibiotic compounds by adsorption using glycerol-based carbon materials, *Chem. Eng. J.*, 2016, **296**, 277–288.

123 F. Ezati, E. Sepehr and F. Ahmadi, The efficiency of nano-TiO_2 and γ-Al_2O_3 in copper removal from aqueous solution by characterization and adsorption study, *Sci. Rep.*, 2021, **11**(1), 1–14.

124 R. Tio, B. Priyadarshini, P. P. Rath, S. S. Behera, S. R. Panda, T. R. Sahoo and P. K. Parhi, Kinetics, Thermodynamics and Isotherm studies on Adsorption of Eriochrome Black-T from aqueous solution using, *IOP Conf. Ser. Mater. Sci. Eng.*, 2018, **310**, 012051.

125 H. Wang, C. Fang, Q. Wang, Y. Chu, Y. Song, Y. Chen and X. Xue, Sorption of tetracycline on biochar derived from rice straw and swine manure, *RSC Adv.*, 2018, **8**, 16260–16268.

126 A. S. Eltaweil, E. M. Abd El-Monaem, A. M. Omer, R. E. Khalifa, M. M. Abd El-Latif and G. M. El-Subruiti, Efficient removal of toxic methylene blue (Mb) dye from aqueous solution using a metal-organic framework (mof) mil-101(fe): Isotherms, kinetics, and thermodynamic studies, *Desalination Water Treat.*, 2020, **189**, 395–407.

127 V. Mishra, Modeling of batch sorber system: kinetic, mechanistic, and thermodynamic modeling, *Appl. Water Sci.*, 2017, **7**(6), 3173–3180.

128 P. Srivastava, S. Goyal and R. Tayade, Ultrasound-assisted adsorption of reactive blue 21 dye on TiO_2 in the presence of some rare earths (La, Ce, Pr & Gd), *Can. J. Chem. Eng.*, 2014, **92**, 41–51.

129 K. Roy, I. A. Khan, B. M. Rizkallah, M. M. Galal, M. E. Matta and K. Alami, Characteristics of Tetracycline Adsorption on Commercial Biochar from Synthetic and Real Wastewater in Batch and Continuous Operations: Study of Removal Mechanisms, Isotherms, Kinetics, Thermodynamics, and Desorption, *Sustainability*, 2023, **15**(10), 8249.

130 Y. E. Du, X. Niu, W. Li, J. An, Y. Liu, Y. Chen, P. Wang, X. Yang and Q. Feng, Microwave-Assisted Synthesis of High-Energy Faceted TiO_2 Nanocrystals Derived from Exfoliated Porous Metatitanic Acid Nanosheets with Improved Photocatalytic and Photovoltaic Performance, *Materials*, 2019, **12**(21), 3614.

131 H. Chen, H.-F. Hsu, H.-Y. Wu -, G. Segal, D. Parkinson, W. Ruu Siah, H. O. Lintang, M. Shamsuddin, L. Yuliati and U. Johor Bahru, High photocatalytic activity of mixed anatase-rutile phases on commercial TiO_2 nanoparticles, *IOP Conf. Ser. Mater. Sci. Eng.*, 2016, **107**, 012005.

132 G. Zerjav, K. Zizek, J. Zavasnik and A. Pintar, Brookite *vs.* rutile *vs.* anatase: What's behind their various photocatalytic activities?, *J. Environ. Chem. Eng.*, 2022, **10**(3), 107722.

133 H. Cheng, J. Wang, Y. Zhao and X. Han, Effect of phase composition, morphology, and specific surface area on

the photocatalytic activity of TiO_2 nanomaterials, *RSC Adv.*, 2014, **4**(87), 47031–47038.

134 Z. Zhao, Z. Li and Z. Zou, A Theoretical study of water adsorption and decomposition on the low-index stoichiometric anatase TiO_2 surfaces, *J. Phys. Chem. C*, 2012, **116**(13), 7430–7441.

135 M. Shen, A. Han, X. Wang, Y. G. Ro, A. Kargar, Y. Lin, H. Guo, P. Du, J. Jiang, J. Zhang, S. A. Dayeh and B. Xiang, Atomic Scale Analysis of the Enhanced Electro- and Photo-Catalytic Activity in High-Index Faceted Porous NiO Nanowires, *Sci. Rep.*, 2015, **5**(1), 1–6.

136 M. Kong, Y. Li, X. Chen, T. Tian, P. Fang, F. Zheng and X. Zhao, Tuning the relative concentration ratio of bulk defects to surface defects in TiO_2 nanocrystals leads to high photocatalytic efficiency, *J. Am. Chem. Soc.*, 2011, **133**(41), 16414–16417.

137 J. Yan, G. Wu, N. Guan, L. Li, Z. Li and X. Cao, Understanding the effect of surface/bulk defects on the photocatalytic activity of TiO_2: Anatase *versus* rutile, *Phys. Chem. Chem. Phys.*, 2013, **15**(26), 10978–10988.

138 H. Zhao, F. Pan and Y. Li, A review on the effects of TiO_2 surface point defects on CO_2 photoreduction with H_2O, *J. Mater.*, 2017, **3**(1), 17–32.

139 H. Zhang, J. Cai, Y. Wang, M. Wu, M. Meng, Y. Tian, X. Li, J. Zhang, L. Zheng, Z. Jiang and J. Gong, Insights into the effects of surface/bulk defects on photocatalytic hydrogen evolution over TiO_2 with exposed {001} facets, *Appl. Catal. B Environ.*, 2018, **220**, 126–136.

140 K. Piler, C. Bahrim, S. Twagirayezu and T. J. Benson, in *Advances in Catalysis*, ed. C. Song, Academic Press Inc., 2020, vol. 66, pp. 109–233.

141 G. H. Safari, M. Hoseini, M. Seyedsalehi, H. Kamani, J. Jaafari and A. H. Mahvi, Photocatalytic degradation of tetracycline using nanosized titanium dioxide in aqueous solution, *Int. J. Environ. Sci. Technol.*, 2015, **12**(2), 603–616.

142 S. Bouafia-Chergui, H. Zemmouri, M. Chabani and A. Bensmaıli, TiO_2-photocatalyzed degradation of tetracycline: kinetic study, adsorption isotherms, mineralization and toxicity reduction, *Desalination Water Treat.*, 2016, **57**(35), 16670–16677.

143 Y. Ma, Q. Peng, M. Sun, N. Zuo, N. Mominou, S. Li, C. Jing and L. Wang, Photocatalytic oxidation degradation of tetracycline over La/Co@TiO_2 nanospheres under visible light, *Environ. Res.*, 2022, **215**, 114297.

144 X. D. Zhu, Y. J. Wang, R. J. Sun and D. M. Zhou, Photocatalytic degradation of tetracycline in aqueous solution by nanosized TiO_2, *Chemosphere*, 2013, **92**(8), 925–932.

145 K. Divakaran, A. Baishnisha, V. Balakumar, K. N. Perumal, C. Meenakshi and R. S. Kannan, Photocatalytic degradation of tetracycline under visible light using TiO_2@sulfur doped carbon nitride nanocomposite synthesized *via in situ* method, *J. Environ. Chem. Eng.*, 2021, **9**(4), 105560.

146 Z. Salmanzadeh-Jamadi, A. Habibi-Yangjeh, S. R. Pouran, X. Xu and C. Wang, Facile fabrication of TiO_2/Bi_5O_7Br photocatalysts for visible-light-assisted removal of

© 2025 The Author(s). Published by the Royal Society of Chemistry

Environ. Sci.: Adv., 2025, **4**, 713–738 | 737

tetracycline and dye wastewaters, *J. Phys. D: Appl. Phys.*, 2022, **55**, 165105.

147 D. Dvoranová, Z. Barbieriková and V. Brezová, Radical Intermediates in Photoinduced Reactions on TiO_2 (An EPR Spin Trapping Study), *Molecules*, 2014, **19**(11), 17279.

148 Q. Chen, K. Wang, G. Gao, J. Ren, R. Duan, Y. Fang and X. Hu, Singlet oxygen generation boosted by Ag–Pt nanoalloy combined with disordered surface layer over TiO_2 nanosheet for improving the photocatalytic activity, *Appl. Surf. Sci.*, 2021, **538**, 147944.

149 Q. Chen, H. Wang, C. Wang, R. Guan, R. Duan, Y. Fang and X. Hu, Activation of molecular oxygen in selectively photocatalytic organic conversion upon defective TiO_2 nanosheets with boosted separation of charge carriers, *Appl. Catal. B Environ.*, 2020, **262**, 118258.

150 J. Peyrton and L. Avérous, Structure-properties relationships of cellular materials from biobased polyurethane foams, *Mater. Sci. Eng. R Rep.*, 2021, **145**, 100608.

151 A. Tewari, S. Gandla, S. Bohm, C. R. McNeill and D. Gupta, Highly Exfoliated MWNT-rGO Ink-Wrapped Polyurethane Foam for Piezoresistive Pressure Sensor Applications, *ACS Appl. Mater. Interfaces*, 2018, **10**(6), 5185–5195.

152 A. C. Mârșolea (Cristea), A. Mocanu, P. O. Stănescu, O. Brincoveanu, C. Orbeci, R. Irodia, C. Pîrvu, A. Dinescu, C. Bobirica and E. Rusen, Synthesis and characterization of polyurethane flexible foams provided from PET derivatives, fly ash, and glass wastes, *Heliyon*, 2023, **9**(12), e23097.

153 R. Ameta, M. S. Solanki, S. Benjamin and S. C. Ameta, in *Advanced Oxidation Processes for Wastewater Treatment: Emerging Green Chemical Technology*, ed. R. Ameta and S. C. Ameta, Elsevier Inc., 2018, pp. 135–175.

154 D. Nunes, A. Pimentel, R. Branquinho, E. Fortunato and R. Martins, Metal oxide-based photocatalytic paper: A green alternative for environmental remediation, *Catalysts*, 2021, **11**(4), 1–30.

155 J. I. Orege, O. Oderinde, G. A. Kifle, A. A. Ibikunle, S. A. Raheem, O. Ejeromedoghene, E. S. Okeke, O. M. Olukowi, O. B. Orege, E. O. Fagbohun, T. O. Ogundipe, E. P. Avor, O. O. Ajayi and M. O. Daramola, Recent advances in heterogeneous catalysis for green biodiesel production by transesterification, *Energy Convers. Manage.*, 2022, **258**, 115406.

156 M. R. Al-Mamun, S. Kader, M. S. Islam and M. Z. H. Khan, Photocatalytic activity improvement and application of UV-TiO_2 photocatalysis in textile wastewater treatment: A review, *J. Environ. Chem. Eng.*, 2019, **7**(5), 103248.

157 M. Hasham Firooz, A. Naderi, M. Moradi and R. R. Kalantary, Enhanced tetracycline degradation with

TiO_2/natural pyrite S-scheme photocatalyst, *Sci. Rep.*, 2024, **14**, 1–20.

158 J. Guo, L. Jiang, J. Liang, W. Xu, H. Yu, J. Zhang, S. Ye, W. Xing and X. Yuan, Photocatalytic degradation of tetracycline antibiotics using delafossite silver ferrite-based Z-scheme photocatalyst: Pathways and mechanism insight, *Chemosphere*, 2021, **270**, 128651.

159 B. Wang, Y. Guo, Q. Li, C. Xin, Y. Tian, W. Zhang and X. Yu, Design of porous ZrO_2 with well-tuned band structures and strong visible-light harvesting via Zn doping for enhanced visible-light photocatalysis, *Chem. Eng. J.*, 2024, **481**, 148489.

160 S. Phanichphant, A. Nakaruk, K. Chansaenpak and D. Channei, Evaluating the photocatalytic efficiency of the $BiVO_4$/rGO photocatalyst, *Sci. Rep.*, 2019, **9**(16091), 1–9.

161 M. Dell'Edera, C. Lo Porto, I. De Pasquale, F. Petronella, M. L. Curri, A. Agostiano and R. Comparelli, Photocatalytic TiO_2-based coatings for environmental applications, *Catal. Today*, 2021, **380**, 62–83.

162 S. Turkoglu, J. Zhang, H. Dodiuk, S. Kenig, J. A. Ratto and J. Mead, Dynamic Wetting Properties of Silica-Poly (Acrylic Acid) Superhydrophilic Coatings, *Polymers*, 2023, **15**(5), 1242.

163 H. T. Nguyen, S. Y. Guo, S. J. You and Y. F. Wang, Visible light driven photocatalytic coating of PAA plasma-grafted PVDF membrane by TiO_2 doped with lanthanum recovered from waste fluorescent powder, *Environ. Eng. Res.*, 2022, **27**(3), 210144.

164 L. M. Anaya-Esparza, N. González-Silva, E. M. Yahia, O. A. González-Vargas, E. Montalvo-González and A. Pérez-Larios, Effect of TiO_2-ZnO-MgO Mixed Oxide on Microbial Growth and Toxicity against *Artemia salina*, *Nanomaterials*, 2019, **9**(7), 992.

165 L. C. Felix, E. J. Folkerts, Y. He and G. G. Goss, Poly(acrylic acid)-coated titanium dioxide nanoparticle and ultraviolet light co-exposure has minimal effect on developing zebrafish (*Danio rerio*), *Environ. Sci.: Nano*, 2017, **4**(3), 658–669.

166 R. Rekulapally, L. N. M. Chavali, M. M. Idris and S. Singh, Toxicity of TiO_2, SiO_2, ZnO, CuO, Au and Ag engineered nanoparticles on hatching and early nauplii of *Artemia sp*, *PeerJ*, 2019, **6**, e6138.

167 L. R. Khoshnood, N. Jaafarzadeh, Sh. Jamili and F. P. Taghavi, Acute toxicity of TiO_2, CuO and ZnO nanoparticles in brine shrimp, *Artemia franciscana*, *Iran. J. Fish. Sci.*, 2017, **16**(4), 1287–1296.

168 Y. Dağlioğlu, İ. Altinok, H. İlhan and M. Sökmen, Determination of the acute toxic effect of ZnO-TiO_2 nanoparticles in brine shrimp (*Artemia salina*), *Acta Biol. Turc.*, 2016, **29**(1), 6–13.